



Minerva Access is the Institutional Repository of The University of Melbourne

Author/s:

Aragon, L;Huang, Y;May, P;Crosier, J;Montoya Duque, E;Connolly, P;Bower, K

Title:

Characterizing precipitation and improving rainfall estimates over the Southern Ocean using ship-borne disdrometer and dual-polarimetric C-band radar

Date:

2024-03-28

Citation:

Aragon, L., Huang, Y., May, P., Crosier, J., Montoya Duque, E., Connolly, P. & Bower, K. (2024). Characterizing precipitation and improving rainfall estimates over the Southern Ocean using ship-borne disdrometer and dual-polarimetric C-band radar. *Journal of Geophysical Research: Atmospheres*, 129 (6), pp.1-21. <https://doi.org/10.1029/2023JD040250>.

Persistent Link:

<https://hdl.handle.net/11343/345446>

License:

[CC BY](#)



RESEARCH ARTICLE

10.1029/2023JD040250

Key Points:

- Different synoptic types across the Southern Ocean exhibit distinctive polarimetric signatures and surface precipitation properties
- Small raindrops of less than one millimeter contribute up to 47% of total accumulation during the Austral warm seasons over the region
- A new formulation for radar rainfall estimates that reflects the large numbers of small drops over the Southern Ocean is proposed

Supporting Information:

Supporting Information may be found in the online version of this article.

Correspondence to:

L. G. B. Aragon,
laragon@student.unimelb.edu.au

Citation:

Aragon, L. G. B., Huang, Y., May, P. T., Crosier, J., Montoya Duque, E., Connolly, P. J., & Bower, K. N. (2024). Characterizing precipitation and improving rainfall estimates over the Southern Ocean using ship-borne disdrometer and dual-polarimetric C-band radar. *Journal of Geophysical Research: Atmospheres*, 129, e2023JD040250. <https://doi.org/10.1029/2023JD040250>

Received 18 OCT 2023

Accepted 24 FEB 2024

Author Contributions:

Conceptualization: L. G. B. Aragon,

Y. Huang, P. T. May, J. Crosier,

E. Montoya Duque, P. J. Connolly

Data curation: L. G. B. Aragon,

Y. Huang, E. Montoya Duque

Formal analysis: L. G. B. Aragon,

Y. Huang, P. T. May, J. Crosier,

E. Montoya Duque, P. J. Connolly,

K. N. Bower

Funding acquisition: Y. Huang






Investigation: L. G. B. Aragon, Y. Huang,

P. T. May, J. Crosier

Methodology: L. G. B. Aragon, Y. Huang,

P. T. May, J. Crosier, P. J. Connolly

Characterizing Precipitation and Improving Rainfall Estimates Over the Southern Ocean Using Ship-Borne Disdrometer and Dual-Polarimetric C-Band Radar

L. G. B. Aragon^{1,2,3} , Y. Huang^{1,2} , P. T. May⁴, J. Crosier^{3,5}, E. Montoya Duque^{1,2} , P. J. Connolly³ , and K. N. Bower³ 

¹School of Geography, Earth and Atmospheric Sciences, The University of Melbourne, Melbourne, VIC, Australia,

²Australian Research Council Centre of Excellence for Climate Extremes, Melbourne, VIC, Australia, ³Centre for Atmospheric Science, Department of Earth and Environmental Sciences, The University of Manchester, Manchester, UK,

⁴School of Earth, Atmosphere and Environment, Monash University, Clayton, VIC, Australia, ⁵National Centre for Atmospheric Science (NCAS), The University of Manchester, Manchester, UK

Abstract Large satellite discrepancies and model biases in representing precipitation over the Southern Ocean (SO) are related directly to the region's limited surface observations of precipitation. To help address this knowledge gap, the study investigated the precipitation characteristics and rain rate retrievals over the remote SO using ship-borne data of the Ocean Rainfall And Ice-phase precipitation measurement Network disdrometer (OceanRAIN) and dual-polarimetric C-band radar (OceanPOL) aboard the Research Vessel (RV) Investigator in the Austral warm seasons of 2016–2018. Seven distinct synoptic types over the SO were analyzed based on their radar polarimetric signatures, surface precipitation phase, and rain microphysical properties. OceanRAIN observations revealed that the SO precipitation was dominated by drizzle and light rain, with small-sized raindrops (diameter <1 mm) constituting up to 47% of total accumulation. Precipitation occurred most frequently over the warm sector of extratropical cyclones, while concentrations of large-sized raindrops (diameter >3 mm) were prominent over synoptic types with colder and more convectively unstable environments. OceanPOL observations complement and extend the surface precipitation properties sampled by OceanRAIN, providing unique information to help characterize the variety of potential precipitation types and associated mechanisms under different synoptic conditions. Raindrop size distributions (DSD) measured with OceanRAIN over the SO were better characterized by analytical DSD forms with two-shape parameters than single-shape parameters currently implemented in satellite retrieval algorithms. This study also revised a rainfall retrieval algorithm for C-band radars to reflect the large amount of small drops and provide improved radar rainfall estimates over the SO.

Plain Language Summary Precipitation is a major component of the hydrologic cycle in high-latitude regions including the remote Southern Ocean (SO). However, large differences continue to exist among current precipitation products in the region, owing in part to the absence of high-quality surface observational records suitable for evaluation across a range of temporal and spatial scales. This work uses two instruments aboard the RV Investigator over the Australian sector of the SO in the Austral warm seasons of 2016–2018: the OceanRAIN disdrometer and OceanPOL radar. We found variability in radar features and surface precipitation properties among seven distinct synoptic conditions over the SO. This work also discussed two important findings related to remote sensing retrievals of SO rain. First, we demonstrated why the rainfall retrieval assumptions in satellite algorithms may need to be refined to account for the unique rainfall properties in the SO. Second, we formulated a new set of equations suitable for shipborne C-band radars in improving rain rate estimates over the region. This work leads toward more accurate, high-resolution estimates of precipitation over the measurement-sparse SO to better understand a range of climatological and meteorological processes in the region.

1. Introduction

Clouds and precipitation over the Southern Ocean (SO) play a critical role in influencing freshwater fluxes, air-sea fluxes, and radiative properties of the region (Caldeira & Duffy, 2000; Pauling et al., 2016; Siems et al., 2022; Wood, 2012). The SO is characterized by fewer land masses and anthropogenic aerosol sources than the Northern Hemisphere, creating a more pristine environment and a distinct mix of cloud and precipitation processes.

© 2024. The Authors.

This is an open access article under the terms of the [Creative Commons Attribution License](https://creativecommons.org/licenses/by/4.0/), which permits use,

distribution and reproduction in any medium, provided the original work is properly cited.

Project administration: Y. Huang
Software: L. G. B. Aragon
Supervision: Y. Huang, P. T. May, J. Crosier, P. J. Connolly
Validation: L. G. B. Aragon
Visualization: L. G. B. Aragon
Writing – original draft: L. G. B. Aragon, Y. Huang, P. T. May, J. Crosier, E. Montoya Duque
Writing – review & editing: L. G. B. Aragon, Y. Huang, P. T. May, J. Crosier, E. Montoya Duque, P. J. Connolly, K. N. Bower

Climate models continue to have large uncertainties in the cloud forcing over the SO, including their inability to reproduce the correct cloud phase, supercooled liquid cloud opacity, and cold cloud processes in the region (Cesana et al., 2022). The poor simulation of cloud forcing in SO, for instance, the abundance of supercooled liquid water in SO clouds, also lead to the significant biases of climate models in representing solar radiation budget over the region (Bodas-Salcedo et al., 2014, 2016; Kay et al., 2016). These large uncertainties and biases have limited the ability of the models to represent important local climate features and their teleconnections such as surface warming, storm activity, and precipitation patterns (Ceppi et al., 2014; McFarquhar et al., 2021; Vergara-Temprado et al., 2018).

Our current knowledge of precipitation over the SO is primarily derived from surface measurements from island sites, satellite remote sensing observations, and reanalysis products (Siems et al., 2022). However, these precipitation products have notable limitations. Historical precipitation records across the SO are rare due to the sparsity of island sites. Orographic effects may have also strongly influenced these records (Lewis et al., 2018; Manton et al., 2020; Siems et al., 2022), limiting their ability to represent precipitation characteristics over the vast open oceans. Indirect measurements of cloud and precipitation from satellite-based products lack calibration for the Southern Hemisphere, which contributes to the large discrepancies among satellite precipitation estimates over the region (McFarquhar et al., 2021; Skofronick-Jackson et al., 2017). Precipitation estimates from reanalysis products strongly depend on model parameterizations and are at scales that do not resolve key processes and, therefore, potentially inherit the climate model biases over the region (Lang et al., 2018; Naud et al., 2014). Further, the reanalysis and satellite estimates do not agree with each other and have large observed errors (Montoya Duque et al., 2023).

In recent years, several observational programs have taken place to address the longstanding knowledge gaps in the nature and variability of precipitation over the SO, including their interaction with other climate components (e.g., McFarquhar et al., 2021). Ship-borne field campaigns, in particular, have provided better spatiotemporal sampling necessary for evaluating satellite-based and model precipitation products over the region. From 2016 to 2018, the Australian Research Vessel (RV) Investigator conducted multiple scientific voyages over the Australian Sector of the SO, enabling comprehensive surface and remote sensing measurements. Routine observations from the RV Investigator along with coordinated field campaigns have led to the recent understanding of the distinct microphysical characteristics of SO precipitation compared with other latitudes (Protat et al., 2019a, 2019b), their variability across different synoptic environments (Lang et al., 2021; Montoya Duque et al., 2022), and case studies of shallow convection and frontal systems over the high-latitude SO (Mace et al., 2023). Observations and analysis are still needed to further understand how the precipitation properties, including rain rate, vary across synoptic types in the SO.

The RV Investigator carries a dual-polarization C-band (5.5 GHz) weather radar called OceanPOL, one of only three ship-borne dual-polarization weather radars in the world and the only one operating over the SO (Protat et al., 2022). OceanPOL provides high-resolution 3-D measurements of precipitation at multiple elevation angles, and its dual-polarization capability enables improved retrievals of hydrometeor species and spatial distributions. Its volumetric scans allow wide coverage of precipitation-size particles that can subsequently reach the surface and are complementary to the profile measurements such as from the vertically-pointing W-band (95 GHz) cloud radar that was also deployed on the RV Investigator for some cruises (e.g., Lang et al., 2021; Mace & Protat, 2018a, 2018b; Montoya Duque et al., 2022). The RV Investigator also carries the Ocean Rainfall And Ice-phase precipitation measurement Network (OceanRAIN), an optical disdrometer that samples the particle size distribution of precipitation along the ship track (Klepp, 2015; Klepp et al., 2018) and can be used to improve the rainfall estimates of OceanPOL.

This study aims to investigate the nature of precipitation and associated properties under various synoptic conditions over the SO. We aim to address the following research questions using the OceanRAIN and OceanPOL data from seven field cruises of the RV Investigator:

1. What are the key precipitation characteristics over the SO, and how do they vary under different synoptic conditions?
2. Are the commonly applied analytical forms of rain drop size distribution (DSD) able to accurately represent the observed DSD over the SO?
3. Can the rainfall properties simulated from OceanRAIN observations be used to improve the rainfall estimates of OceanPOL?

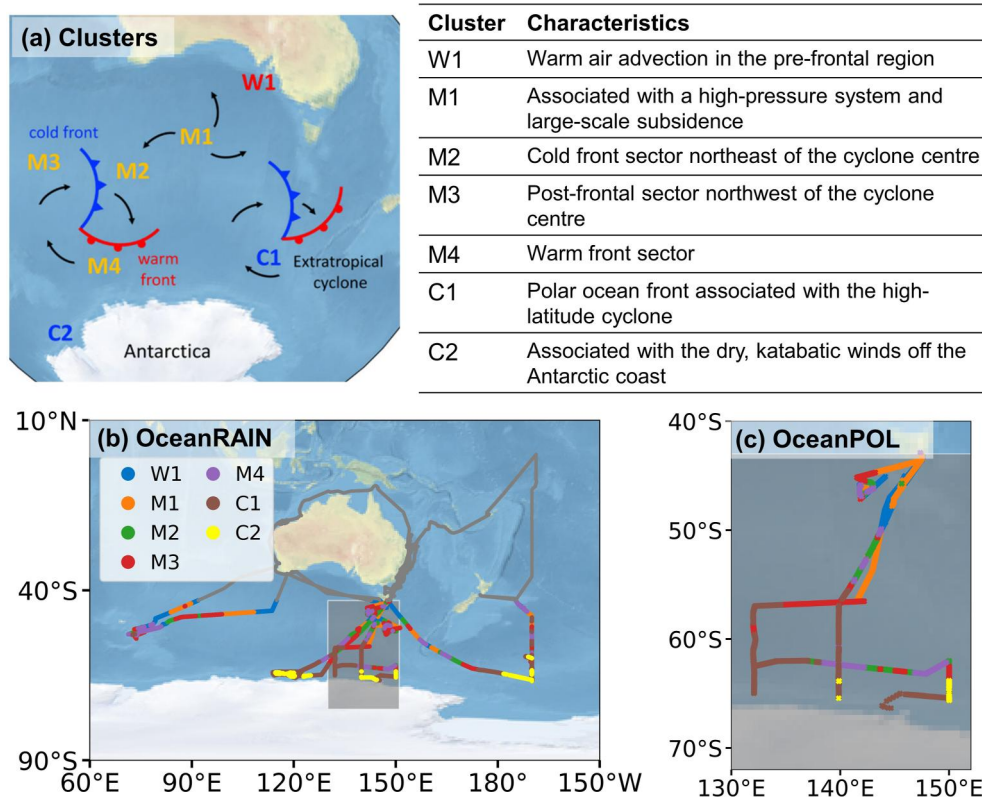


Figure 1. (a) Conceptual illustration of the seven synoptic types over the SO adopted from Truong et al. (2020) and Montoya Duque et al. (2022). Clustered samples of (b) OceanRAIN and (c) OceanPOL from the seven voyages of the RV Investigator in the Austral warm seasons of 2016–2018 (Table S1 in Supporting Information S1). The gray circles in (b) show the OceanRAIN measurements north of 43°S that were discarded from the analysis.

The remainder of the paper is structured as follows: Section 2 provides information about the two instruments and the synoptic type classification. Section 3 provides a sample case of a precipitation event associated with an extratropical cyclone, the bulk analysis of precipitation characteristics, and optimization of the rain rate retrieval algorithms. Finally, Section 4 provides discussion and conclusions.

2. Materials and Methods

2.1. OceanRAIN

OceanRAIN's primary instrument is the ODM470 disdrometer, which counts and sorts precipitation particles into 128 logarithmically distributed size bins from 0.04 to 22.28 mm at one-minute resolution (Klepp, 2015; Klepp et al., 2018). The design of the disdrometer minimizes the impact of artificial small droplets due to splashing, while its algorithm resolves edge effects, coincidence effects from overlapping particles, and precipitation fall velocities. As an initial quality control, the OceanRAIN algorithm automatically removes data from size bins below 0.39 mm, since these smaller droplets are often contaminated with artificial signals from gusty winds and ship propulsion. OceanRAIN identifies the thermodynamic phase of precipitation (liquid, solid, or mixed) following Burdanowitz et al. (2016), which is based on a logistic regression of air temperature, relative humidity, and 99th percentile PSD particle diameter. This algorithm is reported to be more reliable in detecting rain than mixed-phase precipitation and rain-snow transitions at ambient temperatures of -3 and 6°C .

2.1.1. Pre-Processing and Quality Control of OceanRAIN Data

We used OceanRAIN data from seven voyages of the RV Investigator south of 43°S in the Austral warm seasons of 2016–2018 (Figure 1b and Table S1 in Supporting Information S1). Rain, mixed-phase, and ice precipitation samples were used to analyze the surface precipitation frequency and thermodynamic phase under different

synoptic conditions. Rain samples were used to examine the observed DSD and improve the rain rate retrieval algorithm of OceanPOL over the SO.

Recent research using disdrometer observations over Macquarie Island (54.5°S, 158.9°E) showed that small raindrops, less than 1 mm, were significant and contributed ~10% of the total annual precipitation over the island (Tansey et al., 2022). This finding opens up questions on whether and to what extent the small-sized raindrops vary under different synoptic conditions over the broader SO, and if the widely-used analytical forms of DSD can reasonably capture the variability in the observed DSD.

A quality control procedure for rain samples was implemented for this analysis. First, we remove 89 min of rain samples with diameters >8 mm since these samples are likely ice-contaminated or have misclassified precipitation phase, considering that the maximum size of a raindrop is typically around 8 mm (Blanchard & Spencer, 1970; Hobbs & Rangno, 2004). We retained the samples with rain rates of 0.01–100 mm hr⁻¹ and have at least 20 droplets distributed into a minimum of 5 size bins to produce a valid analytical DSD fit (Jaffrain & Berne, 2011; Protat et al., 2019a; Tokay et al., 2013). Altogether, the quality control procedure discarded 33.9% of total minutes of rain observation south of 43°S, with most of these being very light rain and comprising only up to 1% of total rainfall accumulation. The number concentrations for the different diameter bins ($N(D)$; m⁻³ mm⁻¹) were then used to calculate the following rain microphysical variables: liquid water content (LWC; g m⁻³), rain rate (R , mm h⁻¹), total number concentrations (N_t , m⁻³), mass-weighted mean diameter (D_m , mm), and the generalized intercept parameter (N_w , m⁻³ mm⁻¹). For the rain rate calculation, the empirical raindrop size and fall speed relation used by OceanRAIN was also applied (Klepp, 2015), which is based on Atlas and Ulbrich (1974).

2.1.2. Dual-Polarimetric Radar Variables Simulated From OceanRAIN Data

Dual-polarimetric radar variables were calculated from the observed DSD of OceanRAIN using the open-source Python library “PyTMatrix” (Leinonen, 2014), which is based on the T-matrix scattering method (Mishchenko et al., 1996). Previous studies with the micro-rain radar and cloud radar showed good agreement between reflectivity measurements and estimated radar variables from OceanRAIN (Delanoë et al., 2016; Protat et al., 2019a).

The following assumptions in the T-matrix calculations were used for the C-band properties (Protat et al., 2019a, 2019b): (a) the drop shape–size relation from Thurai et al. (2007), (b) drop temperature of 10°C, and (c) canting angles that follow a Gaussian distribution of 0° mean and 10° standard deviation. The following radar variables were then calculated for comparison with the OceanPOL variables to be discussed in the next section: horizontal reflectivity (Z_H ; dBz), differential reflectivity (Z_{DR} ; dB), and specific differential phase (K_{DP} ; ° km⁻¹).

2.2. OceanPOL Radar

OceanPOL has a beamwidth of 1.3°, a range sampling of 125 m (pulse length of 1 microsecond), and a maximum radial distance of 150 km. It typically scans about 14 elevation angles from 0.7° to 32° at 1° azimuth intervals every 6 min (Protat et al., 2022), but the numbers of elevation angles and sampling intervals vary between cruises. The antenna control system of OceanPOL is used to stabilize the antenna for the radar to operate on a ship.

Two OceanPOL data sets have been made available by the Australian Bureau of Meteorology: (a) the Plan Position Indicator (PPI) volume data, and (b) an interpolated and gridded data set using a Barnes (1964) analysis. Here, we use the PPI data to preserve the pixel values of radar observables and avoid smearing of reflectivity features due to interpolation. The following variables from the PPI data were then extracted: Z_H , Z_{DR} , K_{DP} , cross-correlation coefficient (ρ_{HV}), signal-to-noise ratio (SNR), and the hydrometeor classification based on Thompson et al. (2014). The PPI data came from three voyages of the RV Investigator south of 43°S with collocated OceanRAIN measurements (Figure 1c and Table S1 in Supporting Information S1).

The OceanPOL calibration follows the framework applied to operational radars in Australia (Protat et al., 2022; Warren et al., 2018). However, we implemented an additional quality control step to the PPI data to remove, to the extent possible, non-meteorological signals (e.g., sea clutter signals), as well as a Z_{DR} calibration adjustment of -0.4 dB based on our initial analysis of multiple stratiform cases (not shown). We then calculated each radar pixel's refractivity-corrected altitude, distance from the ship, and coordinates using the Python library “Wraddlib” v1.20 (Heistermann et al., 2013). Finally, we retain only radar pixels with the following properties: (a) Z_{DR} between -4 and 4 dB, (b) $\rho_{HV} > 0.85$, and (c) SNR > 10 dB (Figures S1–S3 in Supporting Information S1). We

also limit the analysis to ranges of 10–50 km to minimize the impact of beam broadening (Ryzhkov, 2007). The quality control procedure was necessary and effectively removed the sea clutter signals from the PPI data, but we note that it will have removed some weak meteorological signals (i.e., drizzle and very light precipitation), which will be discussed in detail in Sections 3.4 and 3.5.

2.3. Synoptic Type Classification Using ERA5

The diverse cloud and precipitation properties over the SO are strongly influenced by the synoptic meteorology and thermodynamical environments over this region (Lang et al., 2018; McFarquhar et al., 2021; Montoya Duque et al., 2023; Truong et al., 2020). Truong et al. (2020) identified seven distinct synoptic types over the SO (Figure 1a) from a K-means cluster analysis using upper air soundings from Macquarie Island and recent ship-borne and aircraft campaigns over the region (Figure 1a). These synoptic conditions extend the established cyclone and front compositing methods over the SO by identifying two synoptic types that are unique over the high-latitude SO. The K-means centroids of these seven clusters were used to identify the synoptic types sampled by OceanRAIN (Figure 1b) and OceanPOL (Figure 1c). The synoptic types near the ship location were identified following Montoya Duque et al. (2022) using hourly data from the European Centre for Medium-Range Weather Forecast fifth generation climate reanalysis product (ERA5; Hersbach et al., 2020) (Figure S4 in Supporting Information S1).

3. Results

3.1. Precipitation Over the Warm Sector of an Extratropical Cyclone: A Sample Case

The passage of an extratropical cyclone southwest of Tasmania on 18 January 2018 was sampled by the RV Investigator (Figure 2 and Movie S1). The cyclone was initially located 715 km west of the ship location (143.8°E and 49.9°S) and was moving east-southeastward. The ship remained quasi-stationary, allowing it to record information during several synoptic phases relative to the passage of the cyclone (Figure 2a).

The event started with pre-frontal warm air advection (W1) at the ship location, with north-northwesterly winds, surface temperatures around 10°C, and precipitation developing toward the transition to the warm sector (M4) between 06:30 UTC and 14:30 UTC. The cyclone was closest to the ship (450 km southwest) at 11:50 UTC (Figure 2b), with a surface pressure drop, northerly winds, and increasing precipitation (vertical dashed line in Figure 2a). Precipitation during this period came from the trailing edge of cold optically thick clouds indicated by the low brightness temperatures (<230 K) from the Himawari-8 (Figure 2b) and 0.8° PPI scan of OceanPOL (Figures 2c–2e). A marked increase in Z_H and Z_{DR} and a decrease in ρ_{HV} around the 3.3 km freezing level height (Figures 2f–2h) was detected from the radar vertical cross-sections near the ship at 143–143.7°E. These signals indicate stratiform precipitation with a bright band signature, consistent with steady rain rates below 10 mm hr⁻¹ detected by OceanRAIN (Figure 2a). A brief period of pre-frontal warm air advection was detected at 14:50–15:30 UTC as the ship location moved into the cold sector of the cyclone.

Cold-frontal conditions (M2) were seen from 15:30–19:30 UTC, with westerlies and colder and drier air than in the M4 condition (Figure 2a). Finally, post-frontal conditions (M3) were encountered after 19:30 UTC, as the ship emerged from the cold sector around 670 km northwest of the cyclone center. Light rain (<1 mm hr⁻¹) from multiple open cellular convective clouds was present in the M2 and M3 periods, characterized by widespread patchy shallow (<2 km) radar returns with $Z_H < 20$ dBz (Animation S1). These radar signatures are consistent with previous observations of open mesoscale cellular convection (MCC) in the cold and post-frontal sectors of SO cyclones (Huang et al., 2021; Lang et al., 2022).

The precipitation event presented above illustrated the different cloud organization, polarimetric signatures, and surface variable characteristics including precipitation for the different sectors of the extratropical cyclone. Individual PPI scans also revealed the temporal consistency of precipitation macrostructures across various synoptic conditions.

3.2. Bulk Statistics From OceanPOL and OceanRAIN

To examine further how the precipitation properties vary among synoptic types based on OceanPOL and OceanRAIN observations, we present the bulk statistics of the polarimetric signatures as well as the surface precipitation frequencies, thermodynamic phase, and rain intensities. Contour Frequency by Temperature

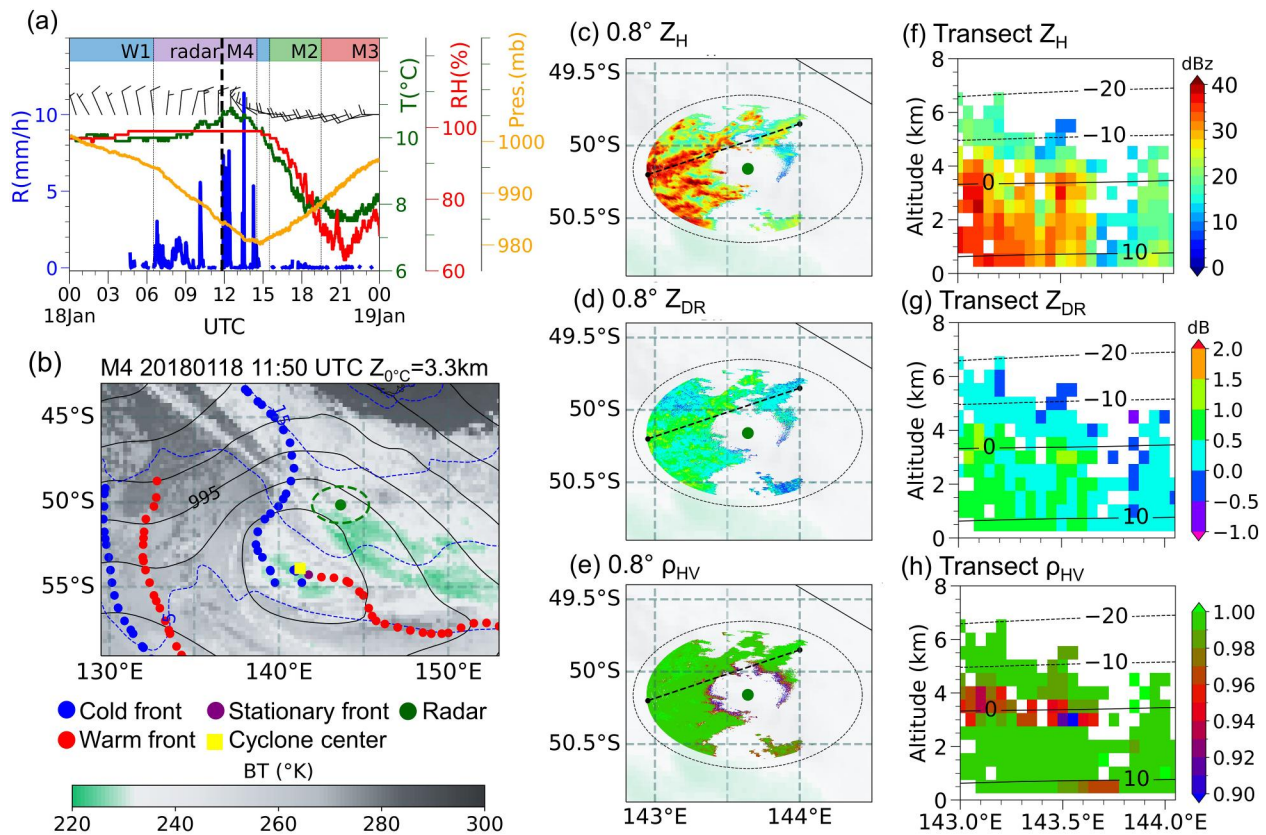


Figure 2. (a) Surface conditions sampled by OceanRAIN on 18 January 2018 as a cyclone traversed east-southeastward of the ship. The evolution of synoptic conditions at the ship location is shown at the top of the panel. The black vertical dashed line denotes the 11:50 UTC timestamp highlighted in the next panels. (b) Synoptic condition around the RV Investigator at 11:50 UTC classified as an M4 cluster. Shown in the panel are the Himawari-8 Channel 13 Brightness temperature (BT); cyclone center and associated fronts from objective identification methods (Berry et al., 2011; Murray & Simmonds, 1991); mean sea level pressure contours (solid black lines), surface temperature contours (dashed blue lines), and freezing level height at the ship location ($Z_{0^{\circ}\text{C}}$ at the title) from the ERA5 data. The green-bordered circle denotes the 150 km radius of OceanPOL. PPI scans of (c) Z_H (d) Z_{DR} , and (e) ρ_{HV} with 0.8° elevation at 11:50 UTC. The black dashed circles denote the 1 km refractivity-corrected altitudes. Vertical profiles of (f) Z_H , (g) Z_{DR} , and (h) ρ_{HV} along the transect line near the ship, denoted by the black dashed diagonal line in (c)–(e). The ERA5 isotherms are also shown. We used each data set’s nearest time offset to 11:50 UTC for (b)–(h) considering their different temporal resolutions. More details are shown in Movie S1.

Diagrams (CFTD; Huang et al., 2015) were used to illustrate the general structure and statistical properties of Z_H and Z_{DR} as a function of temperature (Figure 3). The CFTD is a modified version of the Contour Frequency by Altitude Diagram (Figures S5–S6; Yuter & Houze, 1995). The temperature associated with each precipitation pixel was estimated using linear interpolation to the temperature field of ERA5 at the nearest hour and 3D grid points. We also plot the fractional area of precipitation pixels relative to the PPI scan area at 0.8° elevation. The following temperature regions were highlighted to provide qualitative insights into the precipitation types and microphysical processes aloft: (a) the freezing layer or 0°C line; (b) the Hallett-Mossop temperature range between -8 and -3°C layer (Hallett & Mossop, 1974), which is often associated with mixed-phase clouds and enhanced ice particle production; and (c) the -20 and -10°C layer, where dendritic ice and hexagonal plate growth commonly develops within cold clouds (Bailey & Hallett, 2009; Kennedy & Rutledge, 2011; Williams et al., 2015). The CFTDs were then related to the bulk statistics of surface precipitation from OceanRAIN observation (Figure 4).

The OceanPOL and OceanRAIN data used here was collected over approximately 218 days, with precipitation observed at the ship approximately 20% of the time. The precipitation coverage of the warm front (M4) cluster had the largest areal fraction compared to other synoptic types (first column of Figure 3 and Table 1). This result indicates the widespread precipitation in the warm front sector consistent with the stratiform regime shown in the sample case (Figure 2), and the smaller horizontal scales of precipitation in other synoptic types (e.g., Animation

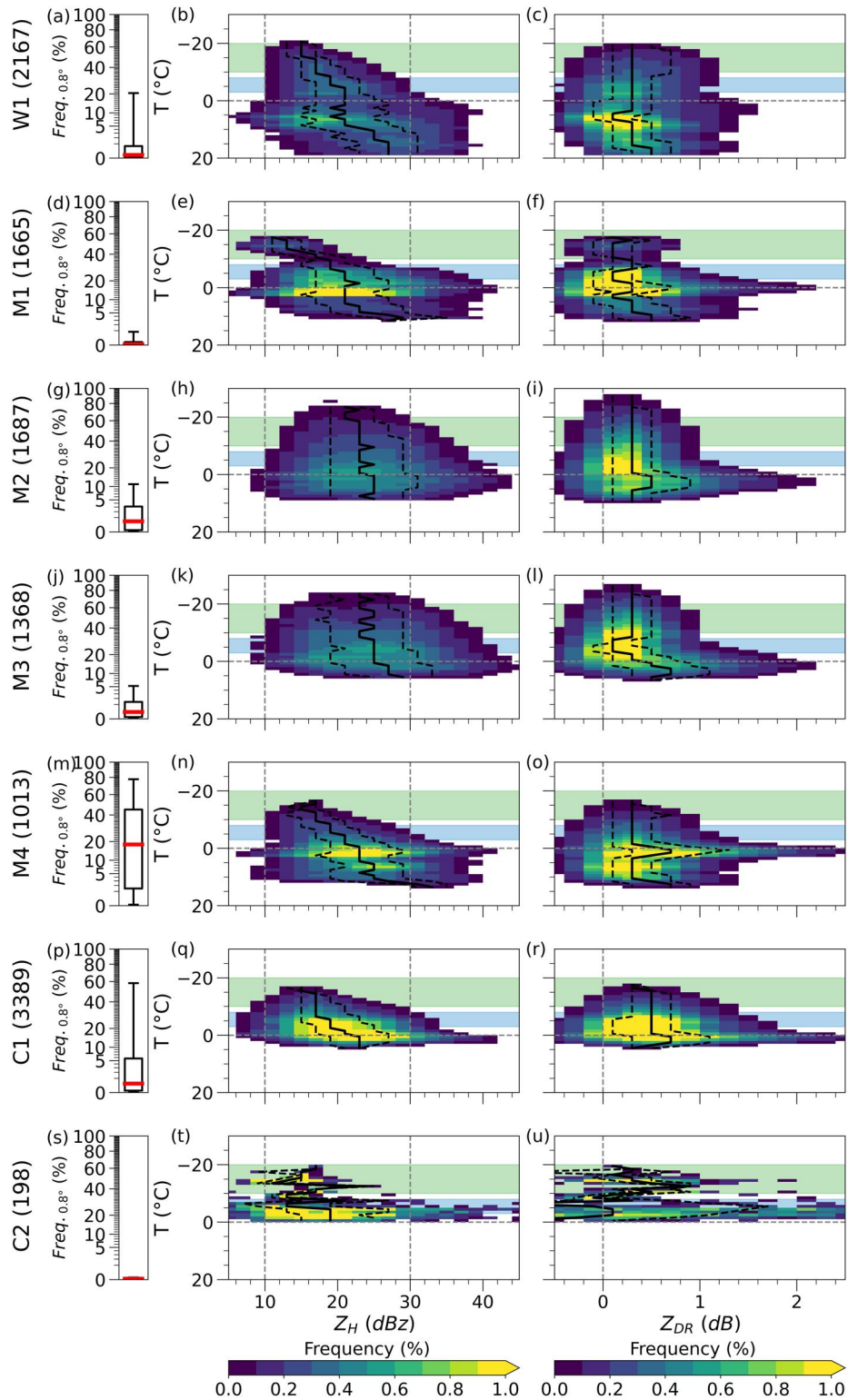


Figure 3. (first column) Boxplots denoting the fraction (%) of precipitation coverage at 0.8° PPI elevation. The number of PPI data for each synoptic type is shown in parenthesis at each row label. Contour Frequency by Temperature Diagram (CFTD) of Z_H (second column) and Z_{DR} (third column) for frequencies above 0.05%. The solid (dashed) black lines along the abscissa show the 50th (25th and 75th) percentiles. The shaded regions indicate possible dendritic growth layer (DGL) commonly occurring at -20 to -10°C (green), and the Hallett-Mossop (H-M) temperature range at -8 to -3°C (blue) often associated with mixed-phase clouds and enhanced ice particle production.

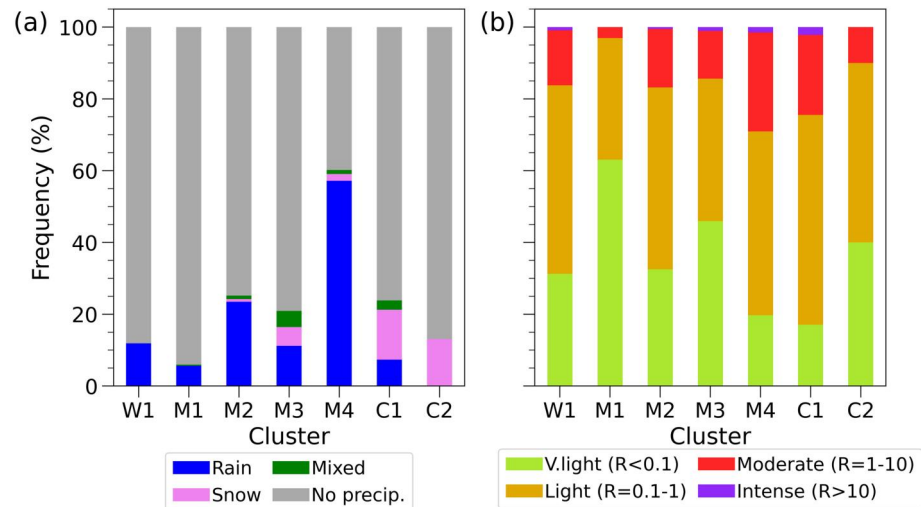


Figure 4. (a) OceanRAIN frequency of precipitation and thermodynamic phase and (b) frequency of very light ($R < 0.1 \text{ mm hr}^{-1}$), light ($0.1-1 \text{ mm hr}^{-1}$), moderate ($1-10 \text{ mm hr}^{-1}$), and intense ($R > 10 \text{ mm hr}^{-1}$) rain rates per synoptic type.

S1). The high variability in precipitation coverage of the M4 cluster is related to the movement of the warm front/sector from the ship location.

The vertical depth of precipitation also varies among synoptic types. Precipitation echoes were often detected up to 7 km during the W1 and M4 cluster periods (Table 1 and Figure S5 in Supporting Information S1). Lower precipitation echo tops were found in other synoptic types including high-pressure conditions (M1), cold fronts (M2), post-frontal sectors (M3), polar ocean fronts (C1), and the dry coastal Antarctic (C2).

The CFTDs for Z_H and Z_{DR} provided insights into the polarimetric signatures and possible microphysical processes related to precipitation particle growth. Fundamentally, Z_H is proportional to the number density and particle sizes, and has higher values for liquid than ice particles. On the other hand, Z_{DR} indicates the particle

Table 1

Precipitation Information From OceanPOL in Terms of the Median and 95th Percentile Values of Precipitation Coverage at 0.8° Elevation (%), Precipitation Echo Top (km), and Ranges of Median Z_H (dBz) and Z_{DR} (dB) Values for the Following Temperature Regions: Dendritic Growth Layer (DGL; -20 to -10°C), Hallett-Mossop (H-M; -8 to -3°C), and Above-Freezing Temperatures ($>0^\circ\text{C}$)

Synoptic type	Median (95th percentile) areal cover (%)	Echo top (km)	Median Z_H (dBz)			Median Z_{DR} (dB)	
			DGL	H-M	$>0^\circ\text{C}$	DGL and H-M	$>0^\circ\text{C}$
W1	0.01 (16.5)	7	15–17	19–21	19–27	0.3	0.1–0.5
M1	0 (0.5)	5.5	11–17	19–21	21–29	0.1–0.3	0.1–0.5
M2	0.4 (10)	5.5	21–23	23–25	23–25	0.3	0.3–0.5
M3	0.09 (2.5)	5.5	23–25	25	25–29	0.1–0.3	0.5–0.7
M4	16 (78)	7	15–17	19–21	23–33	0.3	0.3–0.7
C1	0.1 (53)	5.5	15–17	17–19	23	0.3–0.5	0.3–0.7
C2	0 (<0.1)	3.5	11–23	13–21	–	–1.1–0.9	–

Note. Numerical values found in this table are also shown graphically in Figure 3 and Figure S5 in Supporting Information S1.

shapes, including oblate raindrops ($Z_{DR} > 0$ dB), vertically-oriented particles ($Z_{DR} < 0$ dB), and isotropic particles or a collection of randomly oriented anisotropic particles ($Z_{DR} = 0$ dB). Results showed that low to moderate Z_H (<30 dBz) and Z_{DR} values (<1 dB) were evident at temperatures between -20 and -10°C in the CFTDs of all synoptic types (second and third columns of Figure 3 and Table 1). This radar signature suggests the possible presence of quasi-isotropic ice particles that grow preferentially in water-saturated environments (Giangrande et al., 2016; Griffin et al., 2018; Williams et al., 2015; Wolde & Vali, 2001).

Looking at the polarimetric signatures above the freezing level for the different synoptic types, the W1, M1, and M4 clusters had increasing median Z_H and uniform small median Z_{DR} with increasing temperatures from -20 to -10°C . The steady increase in median Z_H values from the sub-freezing temperatures toward 0°C also indicates the less convective nature of the W1, M1, and M4 clusters. These radar properties suggest the possible presence of active aggregation and/or riming that could dilute the anisotropy and shape diversity of ice particles while increasing in sizes (Kumjian et al., 2022; Ryzhkov et al., 2016; Williams et al., 2015; Wolde & Vali, 2001). On the other hand, the M2, M3, and C1 clusters had broader Z_H distributions and increased presence of $Z_{DR} > 1$ dB extending toward the Hallett-Mossop temperature range of -8 to -3°C . These radar properties suggest diversity in precipitation types and shapes (Giangrande et al., 2016; Keat & Westbrook, 2017; Ryzhkov et al., 2016), and possibly mixed-phase precipitation associated with the convective nature of the three synoptic types. Such a result is seemingly consistent with the limited in-situ and remote data analysis that has shown the Hallett-Mossop ice multiplication process being active in the M3 and C1 clusters (Huang et al., 2017, 2021; Mace et al., 2023; Montoya Duque et al., 2022).

Finally, the largest spread to higher Z_H and Z_{DR} values occurred around 0°C , but was less pronounced in the W1 cluster and stronger in the colder clusters (from M1 to C1 clusters). This radar feature suggests the melting of large ice particles (e.g., aggregates and rimed particles) created in colder thermodynamic environments and is a typical bright-band signature.

At the surface, OceanRAIN sampled mainly rain in most synoptic types (Figure 4a), with 71%–97% of the time being light and very light rain rates (Figure 4b). The M4 cluster had the most precipitation occurrences, the M3 and C1 clusters had relatively higher fractions of mixed and snow precipitation, and the C2 cluster only had snow. We also examined whether the lowest 1 km radar returns from the OceanPOL data can be used to infer qualitatively the surface precipitation phase sampled by OceanRAIN using the ERA5 temperature values assigned to OceanPOL precipitation pixels (Figure S6 in Supporting Information S1). Results showed that the majority of precipitation pixels for most synoptic types were above 0°C . A narrower temperature range near 0°C was found in the precipitation pixels of the M3 and C1 clusters, while the C2 cluster had all precipitation pixels occurring at sub-freezing temperatures. This highlights the general consistency in the precipitation characteristics detected by OceanRAIN and OceanPOL despite their very different sampling strategies.

In summary, the OceanPOL radar features and OceanRAIN surface observations provide useful information to characterize key precipitation properties and potential microphysical processes associated with the seven synoptic types over the SO. The M4 cluster had the largest precipitation coverage and the most frequent surface precipitation. Synoptic types with relatively warmer and less convectively unstable thermodynamic environments (W1, M1, and M4 clusters; Truong et al., 2020) showed clearer polarimetric signatures of potential aggregation/riming processes at sub-freezing temperatures. On the other hand, synoptic types with colder and more convectively unstable environments (M2, M3, and C1 clusters) showed higher variability in polarimetric signatures, suggesting a wide diversity of precipitation types and shapes that are possibly associated with mixed-phase precipitation. There is also a general consistency in the surface thermodynamic phase of precipitation between OceanRAIN and OceanPOL.

3.3. Rain Microphysical Properties

3.3.1. Observed Drop Size Distribution (DSD)

Knowledge of the rain DSDs is central in calculating the bulk rainfall properties and radar variables used for developing the rainfall estimators. Focusing on the rain samples of OceanRAIN, we examine the observed DSD and how the contributions of different raindrop sizes to rainfall accumulation varied among synoptic types (Figure 5). We have excluded the C2 cluster because of its very few rain samples.

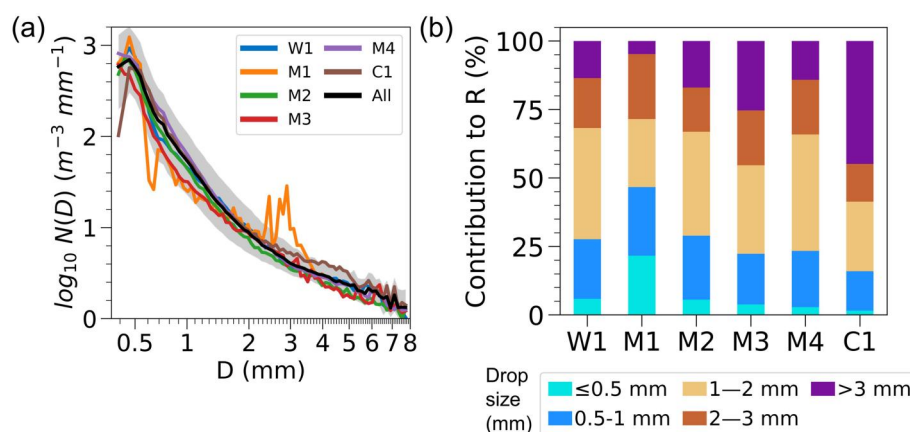


Figure 5. (a) Median values of number concentrations across rain drop size spectra $N(D)$ for each synoptic type and all samples. The shaded region denotes the interquartile ranges from the overall median $N(D)$. (b) Contributions to rainfall accumulation of small-sized (<1 mm; blue bars), mid-sized (1–3 mm; brown bars), and large raindrops (>3 mm; violet bar).

The median values of the number concentrations $N(D)$ for each synoptic type were generally within the interquartile ranges of the total samples (Figure 5a). To examine whether this result is dependent on rain rates, we reduced the DSD variability by scaling the individual $N(D)$ per minute by their respective mass-weighted mean diameter (D_m) and generalized intercept parameter ($\log_{10}N_w$) (Protat et al., 2019a; Testud et al., 2001). The mean scaled $N(D)$ of all synoptic types generally converges into a single scaled $N(D)$ line (not shown), indicating that the median DSD shape found in Figure 5a is within the range of variability of the observed DSD across the SO.

The contributions of the different raindrop sizes to total accumulation were also examined (Figure 5b and Table 2). The contribution of small-sized drops (<1 mm) to rainfall accumulation across synoptic types (16%–47%) is higher than what was previously reported over Macquarie Island in summer (5%; See Table 2 of Tansey et al., 2022). Data processing and instrument differences may have contributed to this discrepancy rather than the fundamental differences in rainfall properties alone. In particular, the higher detection rate of OceanRAIN to small-sized raindrops can be due to its intended design for high sea-state measurements (Klepp, 2015). On the other hand, the Parsivel disdrometer used over Macquarie Island has been documented to undercount small-sized droplets (Löffler-Mang & Joss, 2000; Tokay et al., 2013), which was also validated in Tansey et al. (2022). We also note that the basis for comparing our result (rain only) with the result over Macquarie Island (all precipitation phase) is the dominance of rain during summer over the SO (Figure 4a) from which the OceanRAIN data was obtained.

Looking at the individual clusters, large-size raindrops (>3 mm) had higher contributions to rainfall accumulation in the M3 and C1 clusters. These raindrops possibly came from mixed-phase precipitation aloft (e.g., frozen drops and rimed particles), produced by the convective nature of the said clusters (Figure S4 in Supporting Information S1; Truong et al., 2020). These particles likely retained their large sizes upon reaching the surface because the fall distance from the melting level to the surface was small limiting breakup. The CFTDs of the M3 and C1 clusters support this interpretation, showing broad Z_H and Z_{DR} distributions (Figure 3) and precipitation pixels occurring near 0° C at the lowest 1 km (Figure S6 in Supporting Information S1). We note that the M2 cluster, being associated with cold fronts, features lower concentrations of large-size raindrops. This is likely due to the common presence of multi-layer clouds in this cluster, which are not efficient in developing heavy precipitation (Truong et al., 2020).

In contrast, large-size raindrops made a smaller contribution to rainfall accumulation in the W1, M1, and M4 clusters. The three synoptic types have a less convective nature (Figure S4 in Supporting Information S1; Truong et al., 2020) and thus limited collision-coalescence processes that are typically more active in a convective and turbulent environment. These synoptic types

Table 2
Contributions of Raindrop Sizes to Rainfall Accumulation for Each Synoptic Type From OceanRAIN

Synoptic type	Contribution to rainfall accumulation (%)		
	Small (<1 mm)	Mid-sized (1–3 mm)	Large (>3 mm)
W1	27.6	58.8	13.5
M1	46.7	48.6	4.8
M2	29.0	54.1	17.0
M3	22.3	52.4	25.3
M4	23.4	62.5	14.1
C1	16.0	39.2	44.9

Note. Numerical values found in this table are also shown graphically in Figure 5b for more raindrop size groups.

also have higher freezing level heights, which likely allowed break-up processes of large-sized ice particles created aloft. The high contribution of mid-size raindrops (1–3 mm) to rainfall accumulation in the W1 and M4 clusters may be explained by raindrop growth by coalescence below the freezing layer. These interpretations are particularly consistent with the M4 cluster's CFTD (Figure 3) and sample cases (not shown) that displayed a bright band signature and an increase in Z_{DR} at warmer temperatures, although such polarimetric signatures are less apparent in the W1 and M1 clusters.

3.3.2. Analytical DSD

This section examines how well the commonly used analytical DSD forms capture the observed DSD and rain rates over the SO, given that analytical DSD forms are commonly used in remote sensing precipitation retrievals. Two analytical DSD formulations were evaluated, extending the analysis in Protat et al. (2019a) for different synoptic conditions. The first analytical form (Equation 1) is the Normalized Gamma distribution (Testud et al., 2001; Brangi et al., 2003; referred to as Normalized Gamma fit), which is a 3-parameter function used in the DSD retrievals of the Global Precipitation Measurement (GPM) satellite products (Liao & Meneghini, 2022). Its analytical $N(D)$ is given as

$$N(D) = N_w \frac{\Gamma(4)(3.67 + \mu)^{4+\mu}}{3.67^4 \Gamma(4 + \mu)} \left(\frac{D}{D_m}\right)^\mu \exp\left[-(3.67 + \mu) \frac{D}{D_m}\right] \quad (1)$$

where Γ is the gamma function, μ the shape parameter, N_w the generalized intercept parameter, and D_m is the mass-weighted mean diameter of the DSD.

The second analytical form (Equation 2) is the double-moment Normalized gamma distribution by Delanoë et al. (2014; referred to as Delanoë fit), which has two shape parameters (α and β). It also uses the N_w and D_m as input parameters, and its analytical form is given as:

$$N(D) = N_w \beta \frac{\Gamma(4)}{4^4} \frac{\left[\Gamma\left(\frac{\alpha+5}{\beta}\right)\right]^{(4+\alpha)}}{\left[\Gamma\left(\frac{\alpha+4}{\beta}\right)\right]^{(5+\alpha)}} \left(\frac{D}{D_m}\right)^\alpha \exp\left[-\left(\frac{\Gamma\left(\frac{\alpha+5}{\beta}\right)}{\Gamma\left(\frac{\alpha+4}{\beta}\right)}\right)^\beta \left(\frac{D}{D_m}\right)^\beta\right] \quad (2)$$

The analytical $N(D)$ from the Normalized Gamma and Delanoë fits were calculated by fitting Equations 1 and 2 and their required inputs to individual observed $N(D)$ of OceanRAIN every minute. These values were then used to estimate rain rates that were then compared with OceanRAIN observations (Figure 6). The Delanoë curves fitted the observed DSD (Figure 6b) better than the Normalized Gamma fit (Figure 6a) with lower $N(D)$ biases for small-sized particles. This result is particularly important given the greater significance of small-sized particles in SO rainfall (Figure 5b). The estimated rain rates from the Delanoë fit correlated better with OceanRAIN observation and with less spread compared to the Normalized Gamma fit results, although the Delanoë fit was slightly biased low (Figure 6c).

Satellites such as GPM use the Normalized Gamma fit with a constant shape parameter of $\mu = 3$ (Dual-frequency Precipitation Radar; Seto et al., 2013) and $\mu = 2$ (Combined radar-radiometer; Grecu et al., 2016). However, we found that these constant shape assumptions were higher than the peak shape parameter values of -2 to 1 in all synoptic types (not shown), consistent with what was reported in Protat et al. (2019a). Therefore, the shape parameter assumptions may also contribute to the biases on rainfall retrievals of the GPM satellite products, aside from the abovementioned limitation of the Normalized Gamma fit in retrieving the small-sized particles over the SO.

3.3.3. Rain Microphysical Parameters

The frequency distributions of other rain microphysical variables such as the LWC, $\log_{10}N_t$, D_m , and $\log_{10}N_w$ were also examined (Figure 7). Some of these variables are related to lower DSD moments compared to rain rates and reflectivity, and therefore, are more significantly affected by small-sized raindrops (Raupach et al., 2019). We note that the differences in the frequency distributions for each variable among synoptic types are statistically significant (not shown), suggesting that the synoptic types do not exactly have the same rainfall microphysical

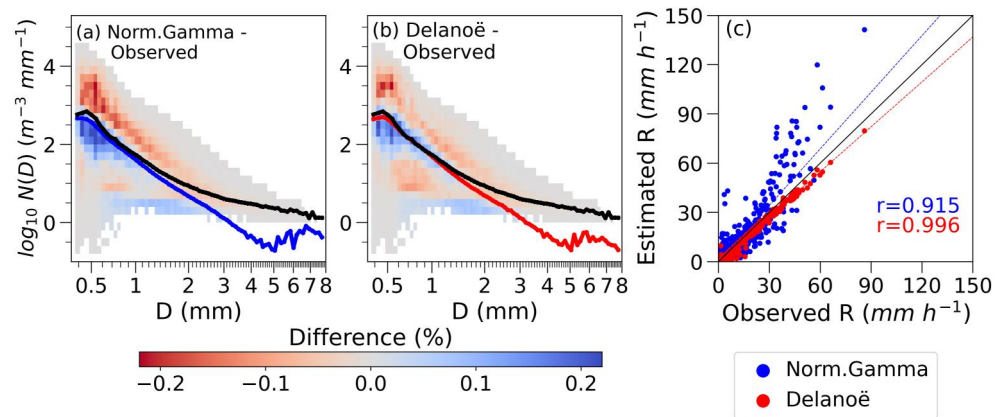


Figure 6. Differences in the joint frequency distributions of analytical DSD using (a) the Normalized Gamma fit and (b) Delanoë fit relative to the observed DSD from all OceanRAIN samples. The lines denote the median $N(D)$ for the observation (black), Normalized Gamma fit (blue in (a)), and Delanoë fit (red in (b)). (c) Scatterplots of estimated rain rates using the Normalized Gamma fit (blue circles) and Delanoë fit (red circles) against OceanRAIN observation. Regression lines for the two gamma fits and their Pearson correlation coefficients (r) with observed rain rates were also shown.

properties consistent with the distinctions in their thermodynamic profiles (Truong et al., 2020) and cloud properties (Montoya Duque et al., 2022).

Results showed that the LWC values below 0.1 g m^{-3} occurred over 80% of the time (Figure 7a), consistent with the dominance of drizzle and light rain across synoptic types (Figure 4b). The overall $\log_{10}N_t$ distribution had a

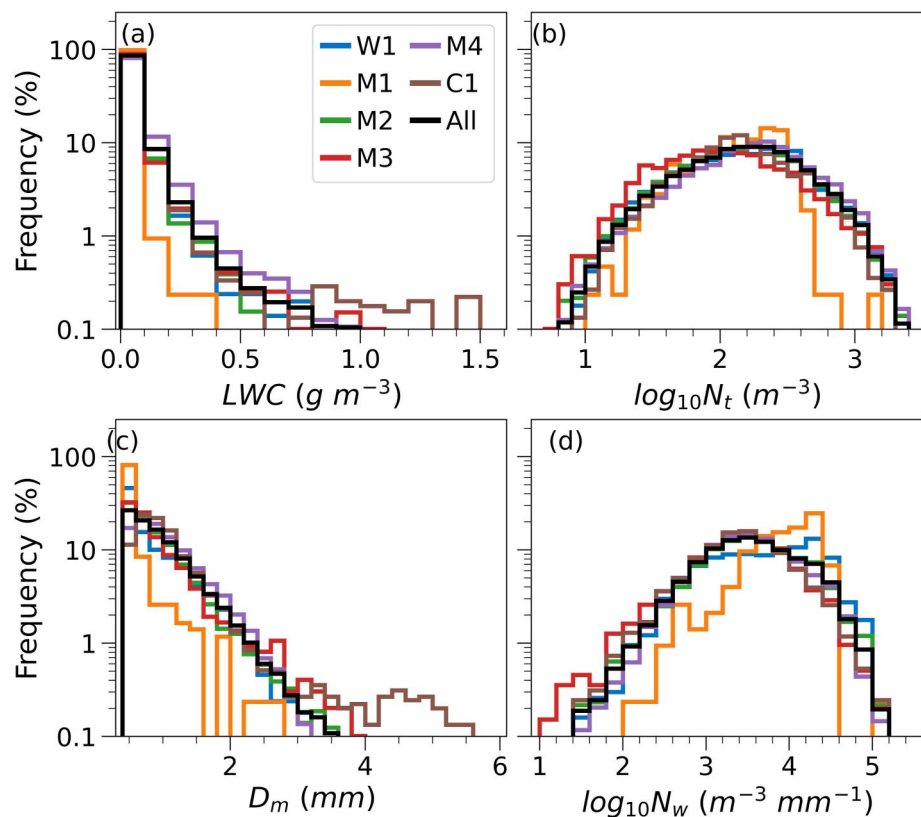


Figure 7. Frequency distributions of (a) liquid water content (LWC), (b) total concentration (N_t), (c) mass-weighted mean diameter (D_m), and (d) generalized number concentration (N_w) for the synoptic types and all samples. These variables were calculated from the DSD observations of OceanRAIN.

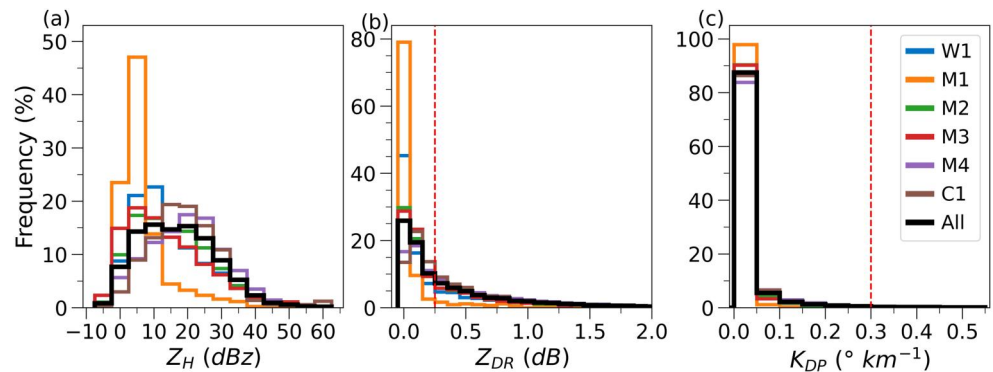


Figure 8. Frequency distributions of OceanRAIN DSD-simulated (a) Z_H , (b) Z_{DR} , and (c) K_{DP} values for the synoptic types and all OceanRAIN data using T-matrix calculations for C-band properties. The red vertical lines in (b) and (c) denote the threshold values of $Z_{DR} = 0.25$ dB and $K_{DP} = 0.3^{\circ} \text{ km}^{-1}$ employed for rainfall retrieval equations.

range of 0.8–3.5 with minimal deviation (Figure 7b), likewise emphasizing the dominant number concentrations of drizzle and light rain in the data. More variability was seen in size-dependent variables such as D_m (Figure 7c) and $\log_{10}N_w$ (Figure 7d), consistent with the different fractional contributions of raindrop sizes to total accumulation (Figure 5b). The M2, M3, and C1 clusters had lower fractions of $D_m < 1$ mm compared with the M1, W1, and M4 clusters (Figure 7c). The joint frequencies of D_m and $\log_{10}N_w$ (not shown) further revealed that these convective clusters had more frequent samples of low $\log_{10}N_w < 3$ and high $D_m > 3$ mm, highlighting the significant contributions of large-sized raindrops to their observed DSD. The overall $\log_{10}N_w$ peaked around $\log_{10}N_w = 3.6$, which is lower than what is typically found in the tropics (e.g., Protat et al., 2019a), and has a spread of 1.4–5.2 for most synoptic types (Figure 7d). The W1 and M1 clusters had higher $\log_{10}N_w$ peaks at $\log_{10}N_w = 4.4$ due to their lower D_m compared with other synoptic types (Figure 7c).

In summary, Section 3.3 examined the rain microphysical properties from OceanRAIN measurements and their relation to OceanPOL polarimetric signatures, thermodynamic profiles, and potential microphysical processes for different synoptic environments. Small-sized raindrops contributed up to 47% of total accumulation across synoptic types. Large-size raindrops, on the other hand, had more contribution to total accumulation in convective clusters (M3 and C1) compared with less convective clusters (W1, M1, and M4). The dominance of drizzle and light rain over the SO are manifested in other rain microphysical variables, also highlighting the importance of small-sized raindrops in the observed DSD over the SO. Given these characteristics, the analytical form by the Delanoë fit based on two shape parameters can better estimate the observed DSD and rain rates, as compared to the Normalized Gamma fit currently implemented in the DSD retrievals of GPM satellite products.

3.4. DSD-Simulated Radar Variables and Updated Rainfall Estimators From OceanRAIN

3.4.1. Z_H , Z_{DR} , and K_{DP} Simulations

The observed DSD from OceanRAIN enables simulations of Z_H , Z_{DR} , and K_{DP} (Bringi et al., 2009; Cifelli et al., 2011; Thompson et al., 2018). Note that Z_H is proportional to the sixth power of raindrop sizes for Rayleigh scatter, Z_{DR} is related to the average particle oblateness, and K_{DP} to the number concentrations of non-spherical particles within a sampling volume (Bringi & Chandrasekar, 2001; Kumjian et al., 2022). Therefore, the DSD-simulated radar variables from OceanRAIN observations provide important “ground-truth” to examine the quantitative rainfall estimates from OceanPOL for the remote SO.

Figure 8 presents the frequency distributions of Z_H , Z_{DR} , and K_{DP} values simulated from the OceanRAIN DSD. The thresholds $Z_{DR} = 0.25$ dB and $K_{DP} = 0.3^{\circ} \text{ km}^{-1}$ incorporated in the figure were based on the rainfall retrieval equations used by OceanPOL, which will be discussed in the next sub-section. The Z_H distributions of most synoptic types were skewed to low values of $Z_H < 20$ dBz (Figure 8a). $Z_{DR} > 0.25$ dB occurred only 44% of the time (Figure 8b), which is lower than what was found in the tropics (57%) reflecting the smaller D_m values. $K_{DP} > 0.3^{\circ} \text{ km}^{-1}$ was virtually absent over the SO (Figure 8c), while it was relatively common in the tropics (11%; Thompson et al., 2018). These results illustrate that an optimized set of radar-based rainfall estimators will better capture SO rainfall.

Table 3

Radar Rainfall Estimators for C-Band Properties Based on Thompson et al. (2018; TH18) Developed Over the Tropical Oceans and OceanRAIN Data Over the SO Derived in This Study (SO23)

Criteria	TH18	SO23
$K_{DP} \leq 0.3$ and $Z_{DR} \leq 0.25$	$R(z_H) = 0.021 z^{0.72}$	$R(z_H) = 0.016 z^{0.846}$
$K_{DP} \leq 0.3$ and $Z_{DR} > 0.25$	$R(z_H, \zeta_{DR}) = 0.0086 z^{0.91} \zeta_{DR}^{-4.21}$	$R(z_H, \zeta_{DR}) = 0.011 z^{0.825} \zeta_{DR}^{-3.055}$
$K_{DP} > 0.3$ and $Z_{DR} \leq 0.25$	$R(K_{DP}) = 30.62 K_{DP}^{0.78}$	$R(K_{DP}) = 16.171 K_{DP}^{0.742}$
$K_{DP} > 0.3$ and $Z_{DR} > 0.25$	$R(K_{DP}, \zeta_{DR}) = 45.70 K_{DP}^{0.88} \zeta_{DR}^{-1.67}$	$R(K_{DP}, \zeta_{DR}) = 24.199 K_{DP}^{0.827} \zeta_{DR}^{-0.488}$

Note. The z_H and ζ_{DR} are the linear versions of Z_H and Z_{DR} , given by $10^{0.1 Z_H}$ and $10^{0.1 Z_{DR}}$, respectively.

3.4.2. Updated Rainfall Estimators for the SO (SO23)

The current rainfall retrieval algorithm used for the OceanPOL data sets is based on Thompson et al. (2018; hereafter TH18). TH18 has four rainfall estimators with different combinations of radar variables based on K_{DP} and Z_{DR} thresholds (second column of Table 3). The coefficients of these equations were derived from the DSD over the tropical ocean, and we have updated these to reflect the DSD characteristics observed by OceanRAIN over the SO (hereafter SO23; third column of Table 3). The K_{DP} and Z_{DR} thresholds were retained, since these values are associated with statistical uncertainty rather than detailed microphysics (Thompson et al., 2018). The $R(z_H)$ and $R(z_H, \zeta_{DR})$ are used mainly to estimate very light to moderate rain rates, and $R(K_{DP})$ and $R(K_{DP}, \zeta_{DR})$ to heavier rain (Cifelli et al., 2011; Thompson et al., 2018). We also performed a k -fold cross-validation (Kohavi, 1995) using $k = 10$ iterative folds for training and validation of OceanRAIN data to confirm the robustness of SO23 against potential coefficient overfitting.

The observed rain rates were first categorized into different estimators depending on their simulated Z_{DR} and K_{DP} values. Then, we examined how frequently the different estimators were used (Figure 9a) and their contributions to rainfall accumulation (Figure 9b). The $R(z_H)$ was used about 56% of the time for the SO rainfall (Figure 9a). On the other hand, moderate rain rates associated with $R(z_H, \zeta_{DR})$ contributed most of the total accumulation (55%; Figure 9b). These frequencies are 1.3 and 2.1 times higher than those in the tropics, signifying how the lower rain rates over the SO made these two rainfall estimators more important compared with the case over the tropics. The contributions of $R(K_{DP}, \zeta_{DR})$ to total accumulation in the M3 and C1 clusters were higher (up to a factor of 5 higher than in other synoptic types; Figure 9b), signifying how the more frequent large-size raindrops in these clusters required the utility of K_{DP} and Z_{DR} values. The $R(K_{DP})$ was not used since there were no OceanRAIN samples with $K_{DP} > 0.3 \text{ km}^{-1}$ and $Z_{DR} < 0.25 \text{ dB}$. Nonetheless, for completeness, we still derived the $R(K_{DP})$ using the samples with $K_{DP} > 0 \text{ km}^{-1}$ for the analysis with OceanPOL (Section 3.5).

The observed rain rates were then compared against the OceanRAIN radar simulation-estimated rain rates of TH18 (Figure 9c) and SO23 (Figure 9d). The $R(z_H)$ estimator of TH18 tends to underestimate OceanRAIN observation (Figure 9c). This result demonstrates that Z_H is higher in the tropics than in SO for a given rain rate due to higher concentrations of large drops in tropical rain. There is also more variance in estimated rain rates using $R(z_H, \zeta_{DR})$ and $R(K_{DP}, \zeta_{DR})$ in TH18, which were notably improved in SO23 (Figure 9d). Estimated rain rates using SO23 correlate better with OceanRAIN observations (Figure 10a), and had lower root-mean-square error (RMSE; Figure 10b) and total accumulation bias (Figure 10c) compared with TH18. Results from k -fold cross-validation (yellow cross) were also more skillful than that of TH18, confirming the robustness of SO23 coefficients in accounting the variability within the OceanRAIN data.

3.5. Comparison Between OceanRAIN and OceanPOL Radar Variables

The DSD-simulated radar variables from OceanRAIN were compared against the quality-controlled radar observables of OceanPOL below 1 km (Figure 11). Only the OceanPOL precipitation pixels classified as rain in its hydrometeor classification product were included in this analysis. Such a comparison allows for a qualitative assessment of the consistency between the two data sets, despite the inherent differences in their instrumentation and sampling procedures. This method helps ensure the applicability of the SO23 rainfall retrieval algorithm to the OceanPOL radar observables.

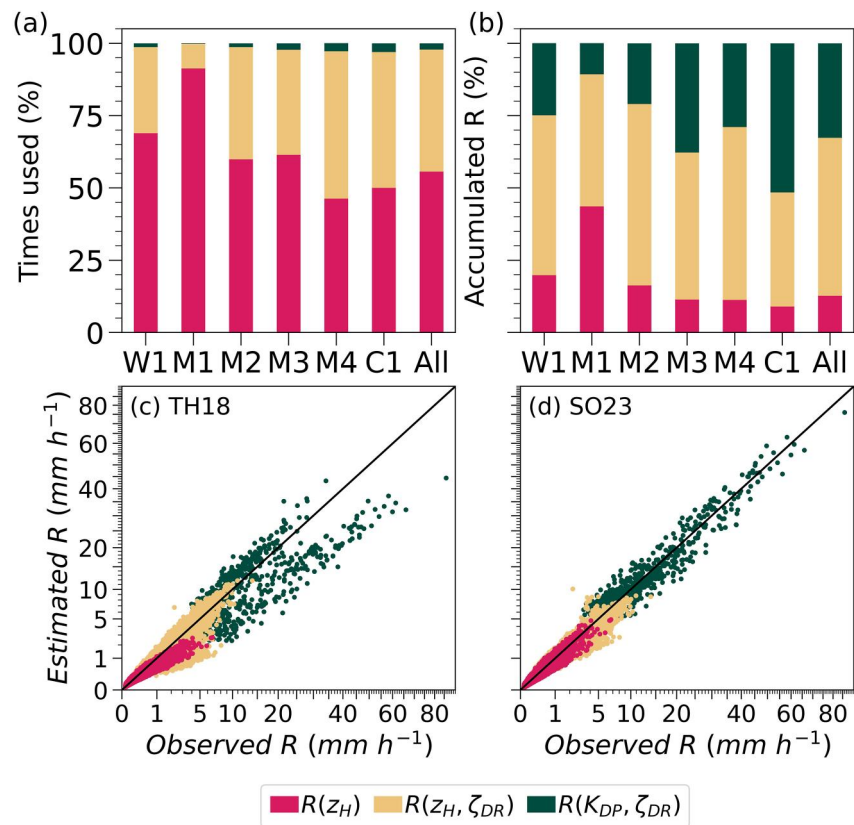


Figure 9. (a) Frequency of times used and (b) contribution to total rainfall accumulation of different rainfall estimators using the OceanRAIN DSD-simulated Z_H , Z_{DR} , and K_{DP} values. Estimated rain rates of (c) TH18 and (d) SO23 retrieval equations (Table 3) relative to OceanRAIN observation. Note that the x- and y-axes were scaled to show lower rain rates.

About 31% of OceanRAIN-simulated Z_H values were below 10 dBz (Figure 11a). This low Z_H value is outside the reliable measurements of OceanPOL (Section 2.2 and Figures S1–S3 in Supporting Information S1). Only the M4 and C1 clusters, which had heavier rain rates, had similar Z_H distributions in OceanPOL and OceanRAIN data (Figure S7 in Supporting Information S1). The OceanPOL's limitation to $Z_H \geq 10$ dBz also resulted in higher Z_{DR}

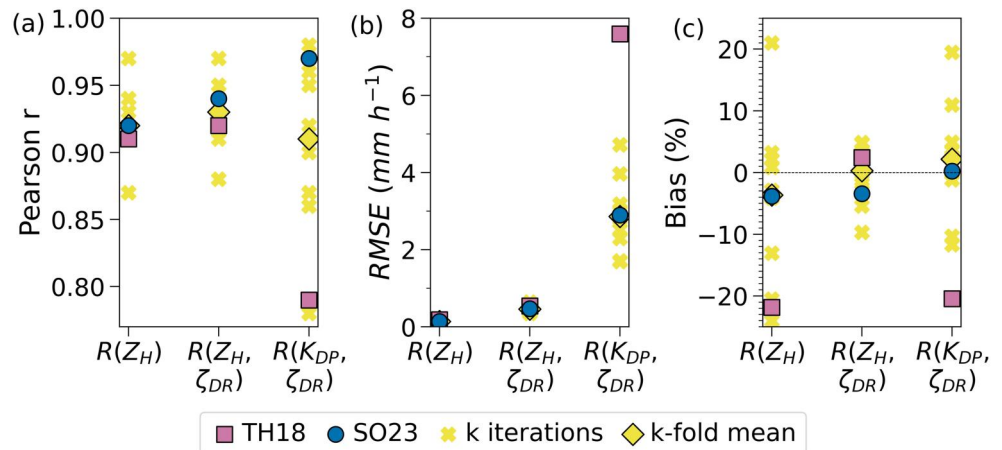


Figure 10. (a) Pearson correlation coefficient (r), (b) root mean squared error (RMSE), and (c) percent bias to total accumulation of OceanRAIN radar simulation-estimated rain rates using TH18 (pink square) and SO23 (blue circle) for $R(Z_H)$, $R(Z_H, \zeta_{DR})$, and $R(K_{DP}, \zeta_{DR})$ relative to OceanRAIN observation. The figure also shows the k-fold cross-validation results for SO23 with $k = 10$ models (yellow cross) and their mean values (yellow diamond) for the different metrics across three rainfall estimators. No OceanRAIN samples satisfied the $R(K_{DP})$ criteria of $K_{DP} > 0.3^\circ \text{ km}^{-1}$ and $Z_{DR} \leq 0.25$ dB.

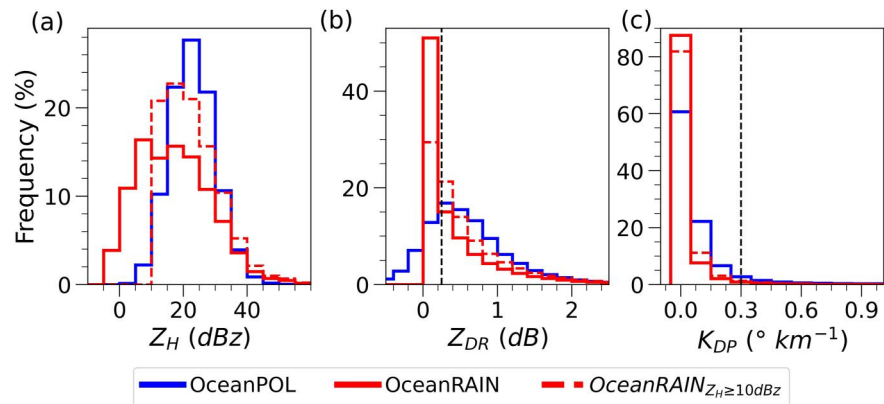


Figure 11. Frequency distributions of (a) Z_H , (b) Z_{DR} , and (c) K_{DP} from all data of OceanPOL (blue line) and OceanRAIN (thick red solid line), and the subset of OceanRAIN data with $Z_H \geq 10$ dBZ (thin red dashed line). The OceanRAIN values were simulated from the surface DSD information using the T-matrix calculation (Section 2.1.2), while the OceanPOL values comprised the quality-controlled rain pixels within 10–50 km at the lowest 1 km altitude (Section 2.2).

(Figure 11b) and K_{DP} (Figure 11c) distributions compared to OceanRAIN-simulated radar values as samples with small drops and low Z_H are preferentially removed. The discrepancies between OceanRAIN and OceanPOL generally reduced after removing the subset of OceanRAIN data with $Z_H < 10$ dBZ (thin red dashed line in Figure 11). This result means that the OceanPOL data is generally similar to OceanRAIN-simulated radar values excluding low Z_H , which gives confidence in using the SO23 algorithm to improve OceanPOL rainfall estimates.

Figure 12 compares the frequency distributions of OceanPOL rainfall estimates using TH18 and SO23 relative to OceanRAIN observations. Note that a direct validation of OceanPOL estimates with OceanRAIN observations is not possible because the OceanRAIN was located in the “blind zone” of the OceanPOL. Both the OceanPOL-estimated rain rates using TH18 and SO23 showed $R > 100$ mm hr^{-1} at $<0.5\%$ of the time (Figure 12a). Such unrealistically high rain rate estimates are a function of measurement errors in OceanPOL variables more than the choice of algorithm. The OceanPOL rain rate estimates using SO23 showed better agreement with observation than the previous algorithm, particularly at the right tail (Figure 12a). This result is highlighted in $R(K_{DP})$ (Figure 12d), where the OceanPOL estimates from SO23 had fewer intense rate rates, and in $R(K_{DP}, \zeta_{DR})$ (Figure 12e), where the OceanPOL estimates from SO23 were closer to observation. OceanPOL estimates for R (z_H) (Figure 12b) and $R(z_H, \zeta_{DR})$ (Figure 12c) are generally comparable to OceanRAIN observations, except for the very light rain rates that were not present in OceanPOL due to its limitation to weak signals.

4. Discussion and Conclusions

This study used the OceanRAIN disdrometer and OceanPOL C-band polarimetric radar to characterize precipitation and improve radar rainfall estimates over the Southern Ocean (SO). Quality-controlled OceanRAIN and OceanPOL data from seven voyages of the RV Investigator in the Austral warm seasons of 2016–2018 were analyzed. The data was divided into seven distinct synoptic types. Key results include:

1. Precipitation over the broad SO during the Austral warm season is dominated by drizzle and rain rates less than 1 mm hr^{-1} . Small-sized raindrops with diameters less than 1 mm contributed 16%–47% of total accumulation across all synoptic types.
2. Precipitation was most frequent in the warm sector (M4) of an extratropical cyclone, while least frequent in high-pressure conditions (M1) and coastal Antarctic-associated (C2) clusters.
3. Larger mass-weighted mean drop diameters were found in synoptic types with colder thermodynamic profiles and more convectively unstable environments such as the cold front sector (M2), post-frontal sector (M3), and ocean polar front at the sub-Antarctic region (C1), as compared to synoptic types with warmer thermodynamic environments, such as the warm-air advection (W1), M1, and M4 clusters.
4. Polarimetric signatures from OceanPOL provided information on the possible presence of quasi-isotropic ice particles within water-saturated environments, more active aggregation/riming processes in less convective

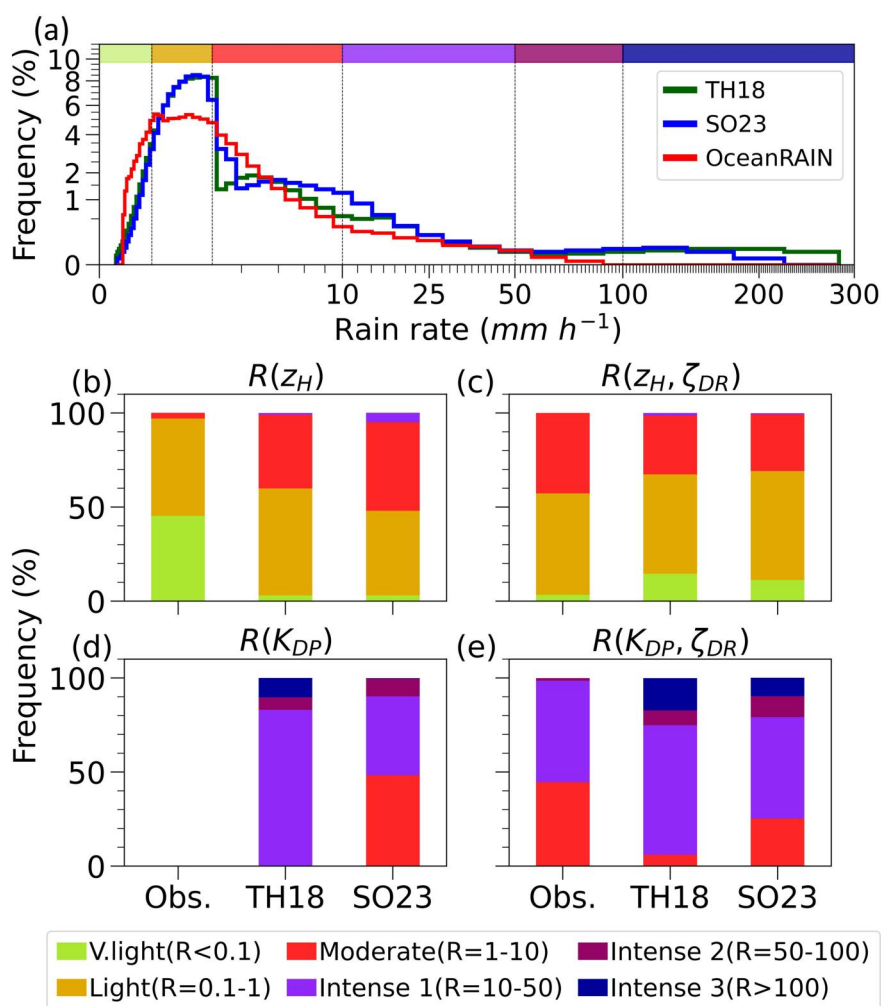


Figure 12. (a) Frequency distributions of rain rates from OceanRAIN observation and OceanPOL estimates using TH18 and SO23 retrieval equations (Table 3). The bars at the top of the panel denote the ranges of categorized rain rates. Note that the x- and y-axes were scaled to highlight lower rain rate and frequency values. (b–e) Frequencies of categorized rain rates from OceanRAIN observation and OceanPOL estimates using TH18 and SO23. There were no OceanRAIN observations that used the $R(K_{DP})$ in (d).

clusters (W1, M1, and M4), and a wider variety of precipitation types and microphysical processes in more convective clusters (M2, M3, and C1).

5. The analytical form of raindrop size distribution (DSD) by Delanoë et al. (2014), which uses a double-moment normalization with two shape parameters better captures the observed DSD and rain rates over the SO compared with the Normalized Gamma distribution currently implemented in GPM satellite retrievals.
6. Radar rainfall estimators developed specifically for the SO using observed DSD from OceanRAIN outperformed the tropics-based retrieval equations (Thompson et al., 2018) currently used by OceanPOL. The stability of the coefficients of the new retrieval equations was also confirmed.

The quality control procedure applied in OceanPOL data, including the $\rho_{HV} > 0.85$ and $SNR > 10$ dB, can be configured depending on the synoptic type that will be examined in future case studies. On the other hand, the Z_{DR} offset of -0.4 dB will also change with future data of OceanPOL, given the ongoing efforts in updating OceanPOL data with improved calibration, K_{DP} estimation, and quality control. We also note the current limitation of OceanPOL in differentiating meteorological signals from noise and sea clutter at $Z_H < 10$ dBz, which highlights the existing challenges in retrieving the bulk properties of drizzle and light precipitation dominant over the SO.

Direct in-situ measurements are essential in validating the polarimetric signatures from OceanPOL. For instance, future studies that incorporate multi-frequency radars collocated on the ship, and combined Doppler spectral analysis with radar polarimetry (e.g., Keat & Westbrook, 2017; Oue et al., 2018) would help in better understanding the variety of mixed and ice precipitation and processes involved in the region. Case studies focusing on the vertical profiles of OceanPOL radar variables can also be done to examine in greater detail which micro-physical processes potentially dominate for the different synoptic types, as well as the other mechanism associated with ice multiplication processes and supercooled liquid drops that are active in SO clouds affecting precipitation. Additionally, the prevalence of mixed precipitation and snow over the high-latitude SO necessitates the retrievals of their bulk properties (e.g., Mace et al., 2023).

Finally, the use of the Normalized gamma distribution (Bringi et al., 2003; Testud et al., 2001) may contribute to the biases of GPM satellite products in retrieving DSD information over the SO. The observed shape parameter over the SO is more likely to decrease and deviate further from the GPM assumptions if the reconstructed DSDs at drizzle mode (Raupach et al., 2019; Thurai et al., 2017) are considered to resolve small raindrops (<0.4 mm) at OceanRAIN's truncation limit. This suggests the potential need for GPM retrievals to refine the shape parameter assumptions or integrate a new analytical DSD form, such as the double moment normalization by Delanoë et al. (2014), for better retrievals of the drizzle-dominant rainfall regime commonly observed over the high-latitude oceans including the SO.

Data Availability Statement

The OceanRAIN version 2 data from the RV Investigator is available upon request to Australia's Bureau of Meteorology through Dr. Alain Protat (alain.protat@bom.gov.au). The other data sets used in this study were obtained from the GADI server of Australia's National Computational Infrastructure (NCI), with the following reference citations: ERA5 (NCI, 2020), Himawari 8/9 (NCI, 2021), and OceanPOL radar (Louf & Protat, 2020). User registration is required for data access.

Acknowledgments

This work was funded by the Melbourne Research Scholarship. Y. Huang was also supported by the Australian Research Council (ARC) Centre of Excellence for Climate Extremes (CE170100023) and ARC discovery grant DP190101362. The authors acknowledge the scientists and technical staff that contributed to the collection, archiving, and post-processing of OceanRAIN and OceanPOL data aboard the RV Investigator, including the CSIRO Marine National Facility (MNF), Australia's National Computational Infrastructure (NCI), and the Bureau of Meteorology. We also sincerely thank Dr. Son Truong for providing the k-means centroids data for synoptic type classification, Dr. Alain Protat for providing OceanRAIN data, and Dr. Valentin Louf for providing details about OceanPOL pre-processing. We also acknowledge the Open-access publishing agreement between Wiley and The University of Melbourne via the Council of Australian University Librarians. Finally, we acknowledge the reviewers for their valuable insights in helping improve the manuscript. Open access publishing facilitated by The University of Melbourne, as part of the Wiley - The University of Melbourne agreement via the Council of Australian University Librarians.

References

- Atlas, D., & Ulbrich, C. (1974). The physical basis for attenuation-rainfall relationships and the measurement of rainfall parameters by combined attenuation and radar methods. *Journal de Recherches Atmospheriques*, 275–298.
- Bailey, M. P., & Hallett, J. (2009). A comprehensive habit diagram for atmospheric ice crystals: Confirmation from the laboratory, AIRS II, and other field studies. *Journal of the Atmospheric Sciences*, 66(9), 2888–2899. <https://doi.org/10.1175/2009JAS2883.1>
- Barnes, S. L. (1964). A technique for maximizing details in numerical weather map analysis. *Journal of Applied Meteorology and Climatology*, 3(4), 396–409. [https://doi.org/10.1175/1520-0450\(1964\)003<0396:ATFMDI>2.0.CO;2](https://doi.org/10.1175/1520-0450(1964)003<0396:ATFMDI>2.0.CO;2)
- Berry, G., Reeder, M. J., & Jakob, C. (2011). A global climatology of atmospheric fronts. *Geophysical Research Letters*, 38(4), L04809. <https://doi.org/10.1029/2010GL046451>
- Blanchard, D. C., & Spencer, A. T. (1970). Experiments on the generation of raindrop-size distributions by drop breakup. *Journal of the Atmospheric Sciences*, 27(1), 101–108. [https://doi.org/10.1175/1520-0469\(1970\)027<0101:EOTGOR>2.0.CO;2](https://doi.org/10.1175/1520-0469(1970)027<0101:EOTGOR>2.0.CO;2)
- Bodas-Salcedo, A., Hill, P. G., Furtado, K., Williams, K. D., Field, P. R., Manners, J. C., et al. (2016). Large contribution of supercooled liquid clouds to the solar radiation budget of the Southern Ocean. *Journal of Climate*, 29(11), 4213–4228. <https://doi.org/10.1175/JCLI-D-15-0564.1>
- Bodas-Salcedo, A., Williams, K. D., Ringer, M. A., Beau, L., Cole, J. N. S., Dufresne, J. L., et al. (2014). Origins of the solar radiation biases over the Southern Ocean in CFMIP2 models. *Journal of Climate*, 27(1), 41–56. <https://doi.org/10.1175/JCLI-D-13-00169.1>
- Bringi, V. N., & Chandrasekar, V. (2001). *Polarimetric Doppler weather radar: Principles and applications*. Cambridge university press. <https://doi.org/10.1017/CBO9780511541094>
- Bringi, V. N., Chandrasekar, V., Hubbert, J., Gorgucci, E., Randeu, W. L., & Schoenhuber, M. (2003). Raindrop size distribution in different climatic regimes from disdrometer and dual-polarized radar analysis. *Journal of the Atmospheric Sciences*, 60(2), 354–365. [https://doi.org/10.1175/1520-0469\(2003\)060<0354:RSDIDC>2.0.CO;2](https://doi.org/10.1175/1520-0469(2003)060<0354:RSDIDC>2.0.CO;2)
- Bringi, V. N., Williams, C. R., Thurai, M., & May, P. T. (2009). Using dual-polarized radar and dual-frequency profiler for DSD characterization: A case study from Darwin, Australia. *Journal of Atmospheric and Oceanic Technology*, 26(10), 2107–2122. <https://doi.org/10.1175/2009JTECHA1258.1>
- Burdanowitz, J., Klepp, C., & Bakan, S. (2016). An automatic precipitation-phase distinction algorithm for optical disdrometer data over the global ocean. *Atmospheric Measurement Techniques*, 9(4), 1637–1652. <https://doi.org/10.5194/amt-9-1637-2016>
- Caldeira, K., & Duffy, P. B. (2000). The role of the southern ocean in uptake and storage of anthropogenic carbon dioxide. *Science*, 287(5453), 620–622. <https://doi.org/10.1126/science.287.5453.620>
- Ceppi, P., Zelinka, M. D., & Hartmann, D. L. (2014). The response of the Southern Hemispheric eddy-driven jet to future changes in shortwave radiation in CMIP5. *Geophysical Research Letters*, 41(9), 3244–3250. <https://doi.org/10.1002/2014GL060043>
- Cesana, G. V., Khadir, T., Chepfer, H., & Chiriacco, M. (2022). Southern ocean solar reflection biases in CMIP6 models linked to cloud phase and vertical structure representations. *Geophysical Research Letters*, 49(22), 1–10. <https://doi.org/10.1029/2022GL099777>
- Cifelli, R., Chandrasekar, V., Lim, S., Kennedy, P. C., Wang, Y., & Rutledge, S. A. (2011). A new dual-polarization radar rainfall algorithm: Application in Colorado precipitation events. *Journal of Atmospheric and Oceanic Technology*, 28(3), 352–364. <https://doi.org/10.1175/2010JTECHA1488.1>
- Delanoë, J., Heymsfield, A. J., Protat, A., Bansemmer, A., & Hogan, R. J. (2014). Normalized particle size distribution for remote sensing application. *Journal of Geophysical Research*, 119(7), 4204–4227. <https://doi.org/10.1002/2013JD020700>

- Delanoë, J., Protat, A., Vinson, J. P., Brett, W., Caudoux, C., Bertrand, F., et al. (2016). BASTA: A 95-GHz FMCW Doppler radar for cloud and fog studies. *Journal of Atmospheric and Oceanic Technology*, 33(5), 1023–1038. <https://doi.org/10.1175/JTECH-D-15-0104.1>
- Giangrande, S. E., Toto, T., Bansemmer, A., Kumjian, M. R., Mishra, S., & Ryzhkov, A. V. (2016). Insights into riming and aggregation processes as revealed by aircraft, radar, and disdrometer observations for a 27 April 2011 widespread precipitation event. *Journal of Geophysical Research: Atmospheres*, 121(10), 5846–5863. <https://doi.org/10.1002/2015JD024537>
- Greco, M., Olson, W. S., Munchak, S. J., Ringerud, S., Liao, L., Haddad, Z., et al. (2016). The GPM combined algorithm. *Journal of Atmospheric and Oceanic Technology*, 33(10), 2225–2245. <https://doi.org/10.1175/JTECH-D-16-0019.1>
- Griffin, E. M., Schuur, T. J., & Ryzhkov, A. V. (2018). A polarimetric analysis of ice microphysical processes in snow, using quasi-vertical profiles. *Journal of Applied Meteorology and Climatology*, 57(1), 31–50. <https://doi.org/10.1175/JAMC-D-17-0033.1>
- Hallett, J., & Mossop, S. C. (1974). Production of secondary ice particles during the riming process. *Nature*, 249(5452), 26–28. <https://doi.org/10.1038/249026a0>
- Heistermann, M., Jacobi, S., & Pfaff, T. (2013). An open source library for processing weather radar data (wradlib). *Hydrology and Earth System Sciences*, 17(2), 863–871. <https://doi.org/10.5194/hess-17-863-2013>
- Hersbach, H., Bell, B., Berrisford, P., Hirahara, S., Horányi, A., Muñoz-Sabater, J., et al. (2020). The ERA5 global reanalysis. *Quarterly Journal of the Royal Meteorological Society*, 146(730), 1999–2049. <https://doi.org/10.1002/qj.3803>
- Hobbs, P. V., & Rangno, A. L. (2004). Super-large raindrops. *Geophysical Research Letters*, 31(13), 2–4. <https://doi.org/10.1029/2004GL020167>
- Huang, Y., Chubb, T., Baumgardner, D., de Hoog, M., Siems, S. T., & Manton, M. J. (2017). Evidence for secondary ice production in Southern Ocean open cellular convection. *Quarterly Journal of the Royal Meteorological Society*, 143(704), 1685–1703. <https://doi.org/10.1002/qj.3041>
- Huang, Y., Protat, A., Siems, S. T., & Manton, M. J. (2015). A-Train observations of maritime midlatitude storm-track cloud systems: Comparing the Southern Ocean against the North Atlantic. *Journal of Climate*, 28(5), 1920–1939. <https://doi.org/10.1175/JCLI-D-14-00169.1>
- Huang, Y., Siems, S. T., & Manton, M. J. (2021). Wintertime in situ cloud microphysical properties of mixed-phase clouds over the Southern Ocean. *Journal of Geophysical Research: Atmospheres*, 126(11), e2021JD034832. <https://doi.org/10.1029/2021JD034832>
- Jaffrain, J., & Berne, A. (2011). Experimental quantification of the sampling uncertainty associated with measurements from PARSIVEL disdrometers. *Journal of Hydrometeorology*, 12(3), 352–370. <https://doi.org/10.1175/2010JHM1244.1>
- Kay, J. E., Wall, C., Yettella, V., Medeiros, B., Hannay, C., Caldwell, P., & Bitz, C. (2016). Global climate impacts of fixing the Southern Ocean shortwave radiation bias in the Community Earth System Model (CESM). *Journal of Climate*, 29(12), 4617–4636. <https://doi.org/10.1175/JCLI-D-15-0358.1>
- Keat, W. J., & Westbrook, C. D. (2017). Revealing layers of pristine oriented crystals embedded within deep ice clouds using differential reflectivity and the copolar correlation coefficient. *Journal of Geophysical Research: Atmospheres*, 122(21), 11737–11759. <https://doi.org/10.1002/2017JD026754>
- Kennedy, P. C., & Rutledge, S. A. (2011). S-band dual-polarization radar observations of winter storms. *Journal of Applied Meteorology and Climatology*, 50(4), 844–858. <https://doi.org/10.1175/2010JAMC2558.1>
- Klepp, C. (2015). The oceanic shipboard precipitation measurement network for surface validation - OceanRAIN. *Atmospheric Research*, 163, 74–90. <https://doi.org/10.1016/j.atmosres.2014.12.014>
- Klepp, C., Michel, S., Protat, A., Burdanowitz, J., Albern, N., Kähner, M., et al. (2018). OceanRAIN, a new in-situ shipboard global ocean surface-reference dataset of all water cycle components. *Scientific Data*, 5(1), 180122. <https://doi.org/10.1038/sdata.2018.122>
- Kohavi, R. (1995). A study of cross-validation and bootstrap for accuracy estimation and model selection. In *Ijcai* (Vol. 14, pp. 1137–1145).
- Kumjian, M. R., Prat, O. P., Reimel, K. J., van Lier-Walqui, M., & Morrison, H. C. (2022). Dual-polarization radar fingerprints of precipitation physics: A review. *Remote Sensing*, 14(15), 1–25. <https://doi.org/10.3390/rs14153706>
- Lang, F., Ackermann, L., Huang, Y., Truong, S. C. H., Siems, S. T., & Manton, M. J. (2022). A climatology of open and closed mesoscale cellular convection over the Southern Ocean derived from Himawari-8 observations. *Atmospheric Chemistry and Physics*, 22(3), 2135–2152. <https://doi.org/10.5194/acp-22-2135-2022>
- Lang, F., Huang, Y., Protat, A., Truong, S. C. H., Siems, S. T., & Manton, M. J. (2021). Shallow convection and precipitation over the Southern Ocean: A case study during the CAPRICORN 2016 field campaign. *Journal of Geophysical Research: Atmospheres*, 126(9), 1–23. <https://doi.org/10.1029/2020JD034088>
- Lang, F., Huang, Y., Siems, S. T., & Manton, M. J. (2018). Characteristics of the marine atmospheric boundary layer over the southern ocean in response to the synoptic forcing. *Journal of Geophysical Research: Atmospheres*, 123(15), 7799–7820. <https://doi.org/10.1029/2018JD028700>
- Leinonen, J. (2014). High-level interface to T-matrix scattering calculations: Architecture, capabilities and limitations. *Optics Express*, 22(2), 1655–1660. <https://doi.org/10.1364/OE.22.001655>
- Lewis, C. J., Huang, Y., Siems, S. T., & Manton, M. J. (2018). Wintertime orographic precipitation over western Tasmania. *Journal of Southern Hemisphere Earth Systems Science*, 68(1), 22–40. <https://doi.org/10.1071/ES18003>
- Liao, L., & Meneghini, R. (2022). GPM DPR retrievals: Algorithm, evaluation, and validation. *Remote Sensing*, 14(4), 1–23. <https://doi.org/10.3390/rs14040843>
- Löffler-Mang, M., & Joss, J. (2000). An optical disdrometer for measuring size and velocity of hydrometeors. *Journal of Atmospheric and Oceanic Technology*, 17(2), 130–139. [https://doi.org/10.1175/1520-0426\(2000\)017<0130:AODFMS>2.0.CO;2](https://doi.org/10.1175/1520-0426(2000)017<0130:AODFMS>2.0.CO;2)
- Louf, V., & Protat, A. (2020). OceanPOL weather radar dataset [Dataset]. *Nuevos Catálogos Industrial & Electrónica*. <https://doi.org/10.25914/5fc4975c7dda8>
- Mace, G. G., Protat, A., Benson, S., & McGlynn, P. (2023). Inferring the properties of snow in southern ocean shallow convection and frontal systems using dual-polarization C-band radar. *Journal of Applied Meteorology and Climatology*, 62(4), 467–487. <https://doi.org/10.1175/JAMC-D-22-0097.1>
- Mace, G. G. J., & Protat, A. (2018a). Clouds over the Southern Ocean as observed from the R/V investigator during CAPRICORN. Part I: Cloud occurrence and phase partitioning. *Journal of Applied Meteorology and Climatology*, 57(8), 1783–1803. <https://doi.org/10.1175/JAMC-D-17-0194.1>
- Mace, G. G. J., & Protat, A. (2018b). Clouds over the Southern Ocean as observed from the R/V investigator during CAPRICORN. Part II: The properties of nonprecipitating stratocumulus. *Journal of Applied Meteorology and Climatology*, 57(8), 1805–1823. <https://doi.org/10.1175/JAMC-D-17-0195.1>
- Manton, M. J., Huang, Y., & Siems, S. T. (2020). Variations in precipitation across the Southern Ocean. *Journal of Climate*, 33(24), 10653–10670. <https://doi.org/10.1175/JCLI-D-20-0120.1>
- McFarquhar, G. M., Bretherton, C. S., Marchand, R., Protat, A., DeMott, P. J., Alexander, S. P., et al. (2021). Observations of clouds, aerosols, precipitation, and surface radiation over the southern ocean. *Bulletin of the American Meteorological Society*, 102(4), E894–E928. <https://doi.org/10.1175/BAMS-D-20-0132.1>

- Mishchenko, M. I., Travis, L. D., & Macke, A. (1996). Scattering of light by polydisperse, randomly oriented, finite circular cylinders. *Applied Optics*, 35(24), 4927–4940. <https://doi.org/10.1364/AO.35.004927>
- Montoya Duque, E., Huang, Y., May, P., & Siems, S. (2023). An evaluation of IMERG and ERA5 quantitative precipitation estimates over the Southern Ocean using shipborne observations. *Journal of Applied Meteorology and Climatology*, 62(11), 1479–1495. <https://doi.org/10.1175/JAMC-D-23-0039.1>
- Montoya Duque, E., Huang, Y., Siems, S., May, P., Protat, A., & McFarquhar, G. (2022). A characterization of clouds and precipitation over the Southern Ocean from synoptic to micro scales during the CAPRICORN field campaigns. *Journal of Geophysical Research: Atmospheres*, 127(17), e2022JD036796. <https://doi.org/10.1029/2022JD036796>
- Murray, R. J., & Simmonds, I. (1991). A numerical scheme for tracking cyclone centres from digital data. Part I: Development and operation of the scheme. *Australian Meteorological Magazine*, 39.
- Naud, C. M., Booth, J. F., & Del Genio, A. D. (2014). Evaluation of ERA-interim and MERRA cloudiness in the Southern Ocean. *Journal of Climate*, 27(5), 2109–2124. <https://doi.org/10.1175/JCLI-D-13-00432.1>
- NCI. (2020). ERA5 dataset [Dataset]. *Nuevos Catálogos Industrial y Electrónica*. <https://doi.org/10.25914/5f48874388857>
- NCI. (2021). Himawari 8/9 full disk observation [Dataset]. *Meteorological Satellite Center*. <https://doi.org/10.25914/61a609f9e7ffa>
- Oue, M., Kollias, P., Ryzhkov, A., & Luke, E. P. (2018). Toward exploring the synergy between cloud radar polarimetry and Doppler spectral analysis in deep cold precipitating systems in the Arctic. *Journal of Geophysical Research: Atmospheres*, 123(5), 2797–2815. <https://doi.org/10.1002/2017JD027717>
- Pauling, A. G., Bitz, C. M., Smith, I. J., & Langhorne, P. J. (2016). The response of the Southern Ocean and Antarctic sea ice to freshwater from ice shelves in an earth system model. *Journal of Climate*, 29(5), 1655–1672. <https://doi.org/10.1175/JCLI-D-15-0501.1>
- Protat, A., Klepp, C., Louf, V., Petersen, W. A., Alexander, S. P., Barros, A., et al. (2019a). The latitudinal variability of oceanic rainfall properties and its implication for satellite retrievals: 1. Drop size distribution properties. *Journal of Geophysical Research: Atmospheres*, 124(23), 13291–13311. <https://doi.org/10.1029/2019JD031010>
- Protat, A., Klepp, C., Louf, V., Petersen, W. A., Alexander, S. P., Barros, A., et al. (2019b). The latitudinal variability of oceanic rainfall properties and its implication for satellite retrievals: 2. The relationships between radar observables and drop size distribution parameters. *Journal of Geophysical Research: Atmospheres*, 124(23), 13312–13324. <https://doi.org/10.1029/2019JD031011>
- Protat, A., Louf, V., Soderholm, J., Brook, J., & Ponsonby, W. (2022). Three-way calibration checks using ground-based, ship-based, and spaceborne radars. *Atmospheric Measurement Techniques*, 15(4), 915–926. <https://doi.org/10.5194/amt-15-915-2022>
- Raupach, T. H., Thurai, M., Bringi, V. N., & Berne, A. (2019). Reconstructing the drizzle mode of the raindrop size distribution using double-moment normalization. *Journal of Applied Meteorology and Climatology*, 58(1), 145–164. <https://doi.org/10.1175/JAMC-D-18-0156.1>
- Ryzhkov, A., Zhang, P., Reeves, H., Kumjian, M., Tschallener, T., Trömel, S., & Simmer, C. (2016). Quasi-vertical profiles—A new way to look at polarimetric radar data. *Journal of Atmospheric and Oceanic Technology*, 33(3), 551–562. <https://doi.org/10.1175/JTECH-D-15-0020.1>
- Ryzhkov, A. V. (2007). The impact of beam broadening on the quality of radar polarimetric data. *Journal of Atmospheric and Oceanic Technology*, 24(5), 729–744. <https://doi.org/10.1175/JTECH2003.1>
- Seto, S., Iguchi, T., & Oki, T. (2013). The basic performance of a precipitation retrieval algorithm for the global precipitation measurement mission's single/dual-frequency radar measurements. *IEEE Transactions on Geoscience and Remote Sensing*, 51(12), 5239–5251. <https://doi.org/10.1109/TGRS.2012.2231686>
- Siems, S. T., Huang, Y., & Manton, M. J. (2022). Southern Ocean precipitation: Toward a process-level understanding. *WIREs Climate Change*, 13(6), e800. <https://doi.org/10.1002/wcc.800>
- Skofronick-Jackson, G., Petersen, W. A., Berg, W., Kidd, C., Stocker, E. F., Kirschbaum, D. B., et al. (2017). The global precipitation measurement (GPM) mission for science and Society. *Bulletin of the American Meteorological Society*, 98(8), 1679–1695. <https://doi.org/10.1175/BAMS-D-15-00306.1>
- Tansey, E., Marchand, R., Protat, A., Alexander, S. P., & Ding, S. (2022). Southern ocean precipitation characteristics observed from CloudSat and ground instrumentation during the macquarie island cloud & radiation experiment (MICRE): April 2016 to March 2017. *Journal of Geophysical Research: Atmospheres*, 127(5), e2021JD035370. <https://doi.org/10.1029/2021JD035370>
- Testud, J., Oury, S., Black, R. A., Amayenc, P., & Dou, X. (2001). The concept of “normalized” distribution to describe raindrop spectra: A tool for cloud physics and cloud remote sensing. *Journal of Applied Meteorology*, 40(6), 1118–1140. [https://doi.org/10.1175/1520-0450\(2001\)040<1118:TCOND>2.0.CO;2](https://doi.org/10.1175/1520-0450(2001)040<1118:TCOND>2.0.CO;2)
- Thompson, E. J., Rutledge, S. A., Dolan, B., Chandrasekar, V., & Cheong, B. L. (2014). A dual-polarization radar hydrometeor classification algorithm for winter precipitation. *Journal of Atmospheric and Oceanic Technology*, 31(7), 1457–1481. <https://doi.org/10.1175/JTECH-D-13-00119.1>
- Thompson, E. J., Rutledge, S. A., Dolan, B., Thurai, M., & Chandrasekar, V. (2018). Dual-polarization radar rainfall estimation over tropical oceans. *Journal of Applied Meteorology and Climatology*, 57(3), 755–775. <https://doi.org/10.1175/JAMC-D-17-0160.1>
- Thurai, M., Gatlin, P., Bringi, V. N., Petersen, W., Kennedy, P., Notaroš, B., & Carey, L. (2017). Toward completing the raindrop size spectrum: Case studies involving 2D-video disdrometer, droplet spectrometer, and polarimetric radar measurements. *Journal of Applied Meteorology and Climatology*, 56(4), 877–896. <https://doi.org/10.1175/JAMC-D-16-0304.1>
- Thurai, M., Huang, G. J., Bringi, V. N., Randeu, W. L., & Schönhuber, M. (2007). Drop shapes, model comparisons, and calculations of polarimetric radar parameters in rain. *Journal of Atmospheric and Oceanic Technology*, 24(6), 1019–1032. <https://doi.org/10.1175/JTECH2051.1>
- Tokay, A., Petersen, W. A., Gatlin, P., & Wingo, M. (2013). Comparison of raindrop size distribution measurements by collocated disdrometers. *Journal of Atmospheric and Oceanic Technology*, 30(8), 1672–1690. <https://doi.org/10.1175/JTECH-D-12-00163.1>
- Truong, S. C. H., Huang, Y., Lang, F., Messmer, M., Simmonds, I., Siems, S. T., & Manton, M. J. (2020). A climatology of the marine atmospheric boundary layer over the southern ocean from four field campaigns during 2016–2018. *Journal of Geophysical Research: Atmospheres*, 125(20), e2020JD033214. <https://doi.org/10.1029/2020JD033214>
- Vergara-Temprado, J., Miltenberger, A. K., Furtado, K., Grosvenor, D. P., Shipway, B. J., Hill, A. A., et al. (2018). Strong control of Southern Ocean cloud reflectivity by ice-nucleating particles. *Proceedings of the National Academy of Sciences of the United States of America*, 115(11), 2687–2692. <https://doi.org/10.1073/pnas.1721627115>
- Warren, R. A., Protat, A., Siems, S. T., Ramsay, H. A., Louf, V., Manton, M. J., & Kane, T. A. (2018). Calibrating ground-based radars against TRMM and GPM. *Journal of Atmospheric and Oceanic Technology*, 35(2), 323–346. <https://doi.org/10.1175/JTECH-D-17-0128.1>
- Williams, E. R., Smalley, D. J., Donovan, M. F., Hollowell, R. G., Hood, K. T., Bennett, B. J., et al. (2015). Measurements of differential reflectivity in snowstorms and warm season stratiform systems. *Journal of Applied Meteorology and Climatology*, 54(3), 573–595. <https://doi.org/10.1175/JAMC-D-14-0020.1>

- Wolde, M., & Vali, G. (2001). Polarimetric signatures from ice crystals observed at 95 GHz in winter clouds. Part II: Frequencies of occurrence. *Journal of the Atmospheric Sciences*, 58(8), 842–849. [https://doi.org/10.1175/1520-0469\(2001\)058<0842:PSFICO>2.0.CO;2](https://doi.org/10.1175/1520-0469(2001)058<0842:PSFICO>2.0.CO;2)
- Wood, R. (2012). Stratocumulus clouds. *Monthly Weather Review*, 140(8), 2373–2423. <https://doi.org/10.1175/MWR-D-11-00121.1>
- Yuter, S. E., & Houze, R. A. (1995). Three-dimensional kinematic and microphysical evolution of Florida cumulonimbus. Part II: Frequency distributions of vertical velocity, reflectivity, and differential reflectivity. *Monthly Weather Review*, 123(7), 1941–1963. [https://doi.org/10.1175/1520-0493\(1995\)123<1941:TDKAME>2.0.CO;2](https://doi.org/10.1175/1520-0493(1995)123<1941:TDKAME>2.0.CO;2)